ANZIAM J. 53(2011), 87–121
doi:10.1017/S1446181112000090

RAYLEIGH–TAYLOR INSTABILITIES IN AXI-SYMMETRIC OUTFLOW FROM A POINT SOURCE

LAWRENCE K. FORBES[1]

(Received 18 October, 2011; revised 3 April, 2012)

Abstract

This paper studies outflow of a light fluid from a point source, starting from an initially spherical bubble. This region of light fluid is embedded in a heavy fluid, from which it is separated by a thin interface. A gravitational force directed radially inward toward the mass source is permitted. Because the light inner fluid is pushing the heavy outer fluid, the interface between them may be unstable to small perturbations, in the Rayleigh–Taylor sense. An inviscid model of this two-layer flow is presented, and a linearized solution is developed for early times. It is argued that the inviscid solution develops a point of infinite curvature at the interface within finite time, after which the solution fails to exist. A Boussinesq viscous model is then presented as a means of quantifying the precise effects of viscosity. The interface is represented as a narrow region of large density gradient. The viscous results agree well with the inviscid theory at early times, but the curvature singularity of the inviscid theory is instead replaced by jet formation in the viscous case. This may be of relevance to underwater explosions and stellar evolution.

2010 *Mathematics subject classification*: 76E17.

Keywords and phrases: interface, instability, curvature singularity, Rayleigh–Taylor flow, spectral methods, spherical coordinates, Boussinesq approximation, vorticity, one-sided outflows.

1. Introduction

Rayleigh–Taylor flows typically occur when a horizontal layer of heavy fluid overlies a lighter fluid layer and there is a narrow interface separating them. Disturbances to the interface are then unstable, and the two fluids attempt to exchange positions, essentially through the formation of fingers that grow at the interface. These unstable flows were initially studied by Rayleigh [43] and Taylor [50], who considered a small sinusoidal disturbance applied to the interface, within the context of linearized theory and for inviscid fluids. It was assumed in that theory that the interface shape

[1]School of Mathematics and Physics, University of Tasmania, Private Bag 37, Hobart, Tasmania 7001, Australia; e-mail: Larry.Forbes@utas.edu.au.

represented only a small disturbance to a horizontal plane, but the linear theory predicts exponential growth of the interface, and so can only be valid for early times. Nonlinear effects become important at later times, and can be responsible for complex mathematical and physical effects in these flows.

The Rayleigh–Taylor instability has been the subject of intensive study, since it occurs in a wide variety of applications. Much of the earlier work on this topic is summarized in review articles by Kull [31] and Sharp [47] and the extensive presentation of Inogamov [28]. The instability occurs in oceanography, where fluid layers overturn through the formation of fingers and plumes, as discussed by Lazier et al. [33]. Rayleigh–Taylor flows are also believed to be of importance in astrophysics, where they could account for the structures seen by McClure-Griffiths et al. [38] in their radio observations of galaxies, and may also play a role in galactic super-bubble formation, as suggested by Low and McCray [36]. A careful observational analysis of 34 planetary nebulae was undertaken by Dgani and Soker [17], who argued that Rayleigh–Taylor instability could account for fragmentation of the halo of the nebula, thus permitting the interstellar medium to penetrate and affect inner regions, too. In astrophysical situations, magnetic fields are expected to have a significant effect on the evolution of the instability, and a review of the magnetohydrodynamics of these situations is presented by Shariff [46]. The Rayleigh–Taylor instability is investigated in planar geometry by Chambers and Forbes [12] for charged fluids in magnetic fields. It is also of interest in geology, and Neil and Houseman [41] have even suggested it as a possible mechanism for the formation of mountains.

Experimental observations of the Rayleigh–Taylor instability in the laboratory have also been undertaken in a variety of situations. In a review article by Berthoud [10] devoted to vapour explosions, the role of this instability in the fragmentation of jets is discussed, and its effect on the break-up of spherical bubbles during violent collapse is analysed by Lin et al. [34] and compared with the predictions of experiments. The effects of magnetic fields in confining some of the unstable spikes produced by Rayleigh–Taylor instability have been studied in a series of experiments undertaken by Kuranz et al. [32] using a laser to initiate the flow. The similarity of this situation to the blast-wave driven instability that might occur in the explosion of a supernova is observed. A recent review by Andrews and Dalziel [3] discusses the development of Rayleigh–Taylor instability, from its early phase of exponential growth to its saturation phase when nonlinear mushroom-shaped bubbles form, and its eventual formation of a mixing layer, and summarizes the results of experimental work for small density difference between the two fluid layers.

In the classical Rayleigh–Taylor instability involving planar flow and two inviscid fluids separated by an infinitesimally thin interface, disturbances are predicted from linearized theory to grow exponentially with time. Eventually, however, nonlinear effects dominate as the interfacial waves grow to finite amplitude, as discussed by Andrews and Dalziel [3]. It is usually observed in simulations that the numerical methods then fail in finite time. This is remarked upon, for example, by Sharp [47].

https://doi.org/10.1017/S1446181112000090 Published online by Cambridge University Press

It is now known from the work of Moore [40] on the related Kelvin–Helmholtz instability that a curvature singularity forms at the interface within finite time. After this critical time, the inviscid model loses its validity, and so the solution then ceases to exist. Cowley et al. [15] confirmed Moore's analysis with an asymptotic argument, for the Kelvin–Helmholtz shear-flow instability, and Baker et al. [6] also demonstrated the use of Moore's analysis in estimating the time to curvature singularity formation in the Rayleigh–Taylor situation. Very recently, the finite-time curvature singularity predicted by Moore [40] has been generalized by Fontelos and De la Hoz [20], and calculated asymptotically both for planar water waves as well as for the Rayleigh–Taylor instability. Baker and Xie [8] have considered the asymptotic behaviour of singularities involved in irrotational models of water waves in deep fluid.

When viscous effects are reintroduced into the model, the curvature singularity predicted by the inviscid theory is instead replaced by a small region of high vorticity, in a flow that is otherwise almost irrotational. This was demonstrated recently in numerical calculations by Forbes [21], but has been understood to be the case for a long time. This patch of vorticity then causes the interface to roll up and form a mushroom-shaped structure. In the related Kelvin–Helmholtz instability, Krasny [29] introduced a "vortex blob" method that effectively replaced the sharp interface between the two fluids with a more diffuse region. His calculations showed that the interface rolled up into the familiar spiral shapes associated with the Kelvin–Helmholtz instability. More recently, Baker and Beale [5] and Baker and Pham [7] have argued that different types of "vortex blob" methods may themselves influence the outcome of the flow, so that a consistent limit may not even be achieved as the effective "blob" size is reduced. This is perhaps to be expected given that these flows are unstable, and so care is evidently needed in the interpretation of these results. Nevertheless, "vortex blob" calculations are in broad agreement with the predictions of fully nonlinear numerical solutions of the Navier–Stokes equations, such as those undertaken by Tryggvason et al. [51].

Extensive direct numerical simulation of the Rayleigh–Taylor instability has been undertaken in the past few decades. A comprehensive review of many of the numerical techniques used in these interfacial flows is given by Scardovelli and Zaleski [45]. An essentially nonoscillatory finite-difference scheme was tested on the Rayleigh–Taylor instability by Shi et al. [48], who demonstrated its ability to compute overturning mushroom-shaped plumes in planar compressible flow. Numerical codes for more complex Rayleigh–Taylor situations have also been devised, such as that reported by Cook and Dimotakis [14], in which provision is made in the modelling for the effects of turbulence. Ramaprabhu et al. [42] and Young and Ham [54] have likewise modelled the turbulent situation in three-dimensional flow. Calder et al. [11] developed a numerical code for simulating astrophysical events, and verified it against experimental data, for the Richtmyer–Meshkov instability (a shock-induced motion of an interface) as well as for the classical Rayleigh–Taylor flow, both of which are believed to be of importance in astronomy. Boundary-integral methods have also been used to compute unstable interface motion, and a review of these techniques

https://doi.org/10.1017/S1446181112000090 Published online by Cambridge University Press

is presented by Hou et al. [27], where their application to the computation of Kelvin–Helmholtz and Rayleigh–Taylor instabilities is discussed.

Rayleigh–Taylor type flows are of interest in geometries other than the purely planar case, and may occur again in astrophysical situations, or in the collapse of a spherical bubble. Epstein [18] points out that these instabilities are also of importance in the inertial confinement of plasmas during fusion experiments. Furthermore, the nonplanar geometry may modify the stability properties of the Rayleigh–Taylor flow through compression and convergence, which is the so-called Bell–Plesset effect. Mikaelian [39] presented a linearized analysis for planar, cylindrical and spherical geometry, and considered the case of concentric shells of fluid undergoing implosion or explosion. This linearized analysis has been extended to the case of compressible fluids by Yu and Livescu [55], and a linearized analysis for both Rayleigh–Taylor and Richtmyer–Meshkov instabilities has been presented by Amendt [2] and applied to the analysis of an implosion in inertial confinement confusion.

Nonlinear effects in curved geometries have also been studied. For the related Richtmyer–Meshkov instability, in which an interface is disturbed by a shock, Matsuoka and Nishihara [37] undertook a weakly nonlinear analysis and compared it against the predictions of a numerical solution for an inviscid two-fluid model, using an approach similar to that of Krasny [29]. The way in which the flow evolves is strongly dependent on the initial conditions, which is perhaps to be expected in these unstable situations, and small initial perturbations of different modes produce very differently shaped outflows at later times. Matsuoka and Nishihara [37] showed results for tri-polar outflows, in which three mushroom-shaped plumes were arranged around the circumference of a cylinder. Very recently, Forbes [22] considered the analogous problem for the Rayleigh–Taylor situation. In that study, a line source ejected a light fluid into a surrounding heavy fluid, so that a cylindrical interface between the fluids moved radially outward as time increased. Small perturbations to the initial fluid speed from the line source then resulted in instabilities at the interface. The inviscid problem with a sharp interface was solved using a spectral method developed for free-surface problems by Forbes et al. [23], and it was shown that curvature singularities were to be expected at the interface within finite time, similar to those predicted by Moore [40] for the planar Kelvin–Helmholtz instability. When viscous effects were included, those points of infinite curvature at the interface were replaced with small regions of very high vorticity, and these ultimately led to the overturning of the interface. Forbes [22] displayed results for several different modes, including a tri-polar outflow similar to that obtained by Matsuoka and Nishihara [37] for the Richtmyer–Meshkov instability.

In the present paper, outflow from a point source located at the origin of a coordinate system is considered, as a model for injection through a narrow pipe in a laboratory experiment, or outflow from a star. The inner injected fluid is lighter than the outer surrounding fluid, and the possibility of an inwardly directed radial gravitation term is included. This is therefore a flow of Rayleigh–Taylor type. For simplicity, the outflow is assumed to be rotationally symmetric about the z-axis, and the instability develops from an initial sphere of radius a. The shape adopted by the outflow is influenced

https://doi.org/10.1017/S1446181112000090 Published online by Cambridge University Press

by initial conditions, and various different Fourier modes may initially be excited. Particularly in the viscous case, however, nonlinearity eventually results in a cascade of energy down to the first Fourier mode, and this dominates the shape of the final outflow, as is illustrated here.

The inviscid model is developed in Section 2, for two immiscible fluids separated by a sharp interface. The linearized solution for this situation is presented in Section 3, and shows the influence of both the Bell–Plesset effect as well as Rayleigh–Taylor instability. A method for including viscous effects in the model is outlined in Section 4, using a Boussinesq approximation for weakly miscible fluids, and the results of calculations are presented and discussed in Section 5. A summary and discussion in Section 6 conclude the paper.

2. The inviscid model

Consider a spherical bubble of fluid of density ρ_1 lying within a second fluid of density ρ_2. The inner fluid (fluid 1) is lighter than the outer one (fluid 2), so that $\rho_1 < \rho_2$. The spherical region of fluid 1 is centred at the origin of a Cartesian coordinate system, and its initial radius is a. A point source located at the origin is turned on impulsively at time $t = 0$, and thereafter it ejects the light fluid (of density ρ_1) at the volume flow rate m. In the inviscid model of this phenomenon, the two fluids are separated by a sharp interface, and for simplicity, it is assumed in this investigation that the flow remains rotationally symmetric about the z-axis.

It is convenient to represent the situation in terms of spherical polar coordinates (r, ϕ, θ), which are related to the Cartesian system by means of the equations

$$\begin{aligned} x &= r \sin\phi \cos\theta, \quad 0 < r < \infty, \\ y &= r \sin\phi \sin\theta, \quad 0 < \phi < \pi, \\ z &= r \cos\phi, \quad 0 < \theta < 2\pi. \end{aligned} \tag{2.1}$$

In this coordinate system, the interface between the two fluids is written in the form $r = R(\phi, t)$. Initially, $R(\phi, 0) = a$, and if the expanding bubble of fluid 1 were to remain spherical, it would have radius

$$A(t) = \left[a^3 + \frac{3mt}{4\pi}\right]^{1/3} \tag{2.2}$$

at all subsequent times. However, since this flow is unstable, any small perturbation to the initial condition will destroy the spherical symmetry (2.2) of the expanding interface.

It is convenient now to make use of nondimensional coordinates and variables, in which all lengths are referenced against the initial radius a of the spherical bubble of fluid 1. Similarly, all times and speeds are referred to the quantities a^3/m and m/a^2, respectively. As each fluid is inviscid and incompressible, each therefore flows irrotationally and so has a velocity potential Φ_j, $j = 1, 2$. These are made

https://doi.org/10.1017/S1446181112000090 Published online by Cambridge University Press

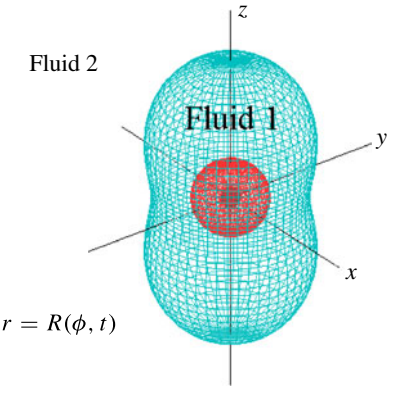

FIGURE 1. A sketch of the dimensionless flow configuration for the inviscid cylindrical Rayleigh–Taylor problem.

dimensionless using the scaling factor m/a. In these nondimensional coordinates, the average radius (2.2) of the expanding bubble of fluid 1 takes the form

$$A(t) = \left[1 + \frac{3t}{4\pi}\right]^{1/3}. \tag{2.3}$$

A sketch of these dimensionless flow coordinates is given in Figure 1. Initially, the interface is the sphere $r = 1$, but at later times the interface forms some different shape dependent upon the initial disturbance made to the original sphere. These two interface configurations are represented in Figure 1. In addition to the details of the initial disturbance, the expanding interface shape is also dependent upon the two dimensionless parameters

$$D = \frac{\rho_2}{\rho_1}, \quad F = \frac{m}{\sqrt{a^3 G\mathcal{M}}}. \tag{2.4}$$

The first of these parameters, D, is the density ratio of the outer to the inner fluid, and for the Rayleigh–Taylor instability of interest, $D > 1$. The second parameter, F, is a type of Froude number based on the gravitational constant G and the mass $\mathcal{M}$ of the star at the origin, and it is assumed that the gravitational force is directed radially inward.

Both the fluids are incompressible and flow irrotationally in the inviscid model, and so the velocity potential Φ_j, $j = 1, 2$, of each fluid satisfies Laplace's equation

$$\nabla^2\Phi_j = \frac{\partial^2\Phi_j}{\partial r^2} + \frac{2}{r}\frac{\partial\Phi_j}{\partial r} + \frac{1}{r^2}\frac{\partial^2\Phi_j}{\partial\phi^2} + \frac{\cot\phi}{r^2}\frac{\partial\Phi_j}{\partial\phi} = 0. \tag{2.5}$$

The velocity vector has components u and w in the radial r and axial ϕ directions, respectively, and these are obtained as the gradient of the potential, in the form

$$u_j = \frac{\partial\Phi_j}{\partial r}, \quad w_j = \frac{1}{r}\frac{\partial\Phi_j}{\partial\phi}. \tag{2.6}$$

https://doi.org/10.1017/S1446181112000090 Published online by Cambridge University Press

There is a mass source at the origin, and so the potential of the lighter inner fluid must therefore behave according to

$$\Phi_1 \to -\frac{1}{4\pi r} \quad \text{as } r \to 0. \tag{2.7}$$

Far away, by conservation of mass, the flow of the outer fluid must likewise resemble outflow from a source at the origin, so that

$$\Phi_2 \to -\frac{1}{4\pi r} \quad \text{as } r \to \infty. \tag{2.8}$$

Since neither fluid may cross the interface at $r = R(\phi, t)$, there are therefore the two kinematic boundary conditions

$$u_j = \frac{\partial R}{\partial t} + \frac{w_j}{R}\frac{\partial R}{\partial \phi}, \quad j = 1, 2, \quad \text{on } r = R(\phi, t) \tag{2.9}$$

that must be obeyed on the interface.

There is also a dynamic condition that must apply at the interface, since the pressures in each fluid must be equal there. Bernoulli's equation holds in each fluid region, and so the pressures p_1 and p_2 are found in the dimensionless forms

$$p_1 = p_\infty - \frac{\partial \Phi_1}{\partial t} - \frac{1}{2}(u_1^2 + w_1^2) + \frac{1}{F^2 r} - \frac{1}{2}\frac{D-1}{(4\pi A^2)^2} + \frac{D-1}{F^2 A}, \tag{2.10}$$

$$p_2 = p_\infty - D\frac{\partial \Phi_2}{\partial t} - \frac{1}{2}D(u_2^2 + w_2^2) + \frac{D}{F^2 r}, \tag{2.11}$$

consistently with Batchelor [9, p. 383]. Here, the parameters D and F are as defined in (2.4) and the function $A(t)$ is the mean radius given by (2.3). The quantity p_∞ is the pressure infinitely far away. The additional terms in the expression for the pressure p_1 in equation (2.10) arise from the fact that the two pressures must be equal at the interface, even for the trivial (unperturbed) solution

$$\Phi_1 = \Phi_2 = -\frac{1}{4\pi r}, \quad R(\phi, t) = A(t)$$

of the flow equations. The requirement that the two pressures in equations (2.10) and (2.11) must remain equal at the interface then gives the dynamical constraint

$$\begin{aligned} D\frac{\partial \Phi_2}{\partial t} - \frac{\partial \Phi_1}{\partial t} + \frac{1}{2}D(u_2^2 + w_2^2) - \frac{1}{2}(u_1^2 + w_1^2) - \frac{D-1}{F^2 r} \\ = \frac{1}{2}\frac{D-1}{(4\pi A^2)^2} - \frac{D-1}{F^2 A} \quad \text{on } r = R(\phi, t) \end{aligned} \tag{2.12}$$

at the moving interface.

A numerical solution is sought to this nonlinear problem, which has the additional feature that it is singular, due to the presence of the source at the origin. This requires

https://doi.org/10.1017/S1446181112000090 Published online by Cambridge University Press

a representation of the two velocity potentials Φ_1 and Φ_2 in a form that identically satisfies Laplace's equations (2.5), the condition (2.7) near the mass source, and (2.8) far away. This is achieved by the series

$$\Phi_1(r,\phi,t) = -\frac{1}{4\pi r} + B_0(t) + \sum_{n=1}^{N} B_n(t) r^n P_n(\cos\phi), \tag{2.13}$$

$$\Phi_2(r,\phi,t) = -\frac{1}{4\pi r} + \sum_{n=1}^{N} C_n(t) r^{-n-1} P_n(\cos\phi). \tag{2.14}$$

In these expressions, the Fourier–Legendre coefficients $B_n(t)$ and $C_n(t)$ are unknown functions of time t, and the symbol $P_n(z)$ denotes the Legendre polynomial of order n and argument z, as presented by Gradshteyn and Ryzhik [26, p. 973]. The shape of the interface $r = R(\phi, t)$ is similarly represented as

$$R(\phi,t) = A(t) + H_0(t) + \sum_{n=1}^{N} H_n(t) P_n(\cos\phi), \tag{2.15}$$

in which the unperturbed radius function $A(t)$ is as defined in equation (2.3). These expressions become exact as the number N of Fourier modes is increased. For later use, it is convenient to define interfacial velocity components U_j and W_j along the interface, using (2.6) and the forms (2.13) and (2.14). This gives functions

$$U_1(\phi,t) = \frac{1}{4\pi R^2} + \sum_{n=1}^{N} n B_n(t) R^{n-1} P_n(\cos\phi), \tag{2.16}$$

$$W_1(\phi,t) = -\sum_{n=1}^{N} B_n(t) R^{n-1} P_n'(\cos\phi)\sin\phi \tag{2.17}$$

in fluid 1, and

$$U_2(\phi,t) = \frac{1}{4\pi R^2} - \sum_{n=1}^{N} (n+1) C_n(t) R^{-n-2} P_n(\cos\phi),$$

$$W_2(\phi,t) = -\sum_{n=1}^{N} C_n(t) R^{-n-2} P_n'(\cos\phi)\sin\phi$$

for the velocity components in fluid 2.

It remains to find the three sets of coefficients $B_n(t)$, $C_n(t)$ and $H_n(t)$ that satisfy the three conditions in (2.9) and (2.12). This is done here using the method of Forbes et al. [23]. The kinematic condition (2.9) in fluid 1 is analysed at the zeroth Fourier mode by multiplying by $R^2\sin\phi$ and integrating over the interval $0 < \phi < \pi$. It may be shown from the definitions (2.16) and (2.17) and integration by parts that

$$\int_0^\pi R\frac{\partial R}{\partial \phi} W_1 \sin\phi\, d\phi = \int_0^\pi R^2 U_1 \sin\phi\, d\phi - \frac{1}{2\pi},$$

https://doi.org/10.1017/S1446181112000090 Published online by Cambridge University Press

so that, at the zeroth order, the kinematic condition in fluid 1 gives rise to the condition

$$\int_0^\pi R^2 \frac{\partial R}{\partial t} \sin\phi \, d\phi = \frac{1}{2\pi}. \tag{2.18}$$

The representation (2.15) of the interface shape is used in the result (2.18), and gives rise to the condition

$$M_{00} H_0'(t) + \sum_{n=1}^{N} M_{0n} H_n'(t) = \frac{1}{2\pi} - \frac{M_{00}}{4\pi A^2(t)}. \tag{2.19}$$

In expression (2.19), the quantity $A(t)$ is the undisturbed radius function defined in equation (2.3). The remaining intermediate functions in this relation are

$$M_{0n}(t) = \int_0^\pi R^2(\phi, t) P_n(\cos\phi) \sin\phi \, d\phi, \quad n = 0, 1, \ldots, N. \tag{2.20}$$

The higher-order Fourier modes are similarly obtained by multiplying condition (2.9) for fluid 1 by the functions $R^2 P_\ell(\cos\phi) \sin\phi$, $\ell = 1, 2, \ldots, N$, and integrating over the interval $0 < \phi < \pi$. After integration by parts, and making use of the definitions (2.16) and (2.17), the higher modes for the kinematic condition in the inner fluid yield the system of differential equations

$$M_{\ell 0} H_0'(t) + \sum_{n=1}^{N} M_{\ell n} H_n'(t) = \sum_{n=1}^{N} S_{\ell n}^{(1)} B_n(t) - A'(t) M_{\ell 0}, \quad \ell = 1, 2, \ldots, N. \tag{2.21}$$

In expression (2.21), the intermediate functions are again as defined in (2.20), along with the additional quantities

$$M_{\ell n}(t) = \int_0^\pi R^2(\phi, t) P_\ell(\cos\phi) P_n(\cos\phi) \sin\phi \, d\phi. \tag{2.22}$$

The symbol $A(t)$ denotes the unperturbed radius (2.3) and $A'(t) = 1/(4\pi A^2(t))$ is its derivative. The right-hand side of this expression also involves the quantity

$$S_{\ell n}^{(1)}(t) = \frac{1}{(n+1)} \int_0^\pi R^{n+1}(\phi, t) P_n'(\cos\phi) P_\ell'(\cos\phi) \sin^3\phi \, d\phi \tag{2.23}$$

as a further intermediate variable.

In analysing the second kinematic condition in the system (2.9), it is convenient to follow the algorithm of Forbes et al. [23] and Forbes and Hocking [25], by replacing the second kinematic condition with the difference of the two. The contribution from the zeroth Fourier mode is obtained by multiplying by $R^2 \sin\phi$ and integrating over $0 < \phi < \pi$ as previously. After integration by parts and making use of the definitions (2.16) and (2.17) it may be shown that this zeroth mode is satisfied identically.

https://doi.org/10.1017/S1446181112000090 Published online by Cambridge University Press

The higher-order modes are similarly obtained by multiplying the difference of the two kinematic conditions by the functions $R^2 P_\ell(\cos\phi)\sin\phi$, for $\ell = 1, 2, \ldots, N$, and integrating as previously. This gives the system

$$\int_0^\pi R^2(U_2 - U_1)P_\ell(\cos\phi)\sin\phi\, d\phi = \int_0^\pi R(W_2 - W_1)\frac{\partial R}{\partial\phi}P_\ell(\cos\phi)\sin\phi\, d\phi, \quad \ell = 1, 2, \ldots, N. \tag{2.24}$$

The term on the right-hand side of equation (2.24) is integrated by parts, and after a little algebra the equations reduce to

$$\sum_{n=1}^N S^{(1)}_{\ell n}(t)B_n(t) + \sum_{n=1}^N S^{(2)}_{\ell n}(t)C_n(t) = 0, \quad \ell = 1, 2, \ldots, N, \tag{2.25}$$

in which the intermediate quantity $S^{(1)}_{\ell n}$ in the first sum has been defined in (2.23). The function in the second sum is written as

$$S^{(2)}_{\ell n}(t) = \frac{1}{n}\int_0^\pi R^{-n}(\phi, t)P_n'(\cos\phi)P_\ell'(\cos\phi)\sin^3\phi\, d\phi. \tag{2.26}$$

The result (2.25) has an elegant form, but is not convenient for the present application, since it would result in a system of differential algebraic equations when combined with other conditions such as (2.21) at the interface. However, a strength of the present spectral approach is that the identity (2.25) can be differentiated directly with respect to time t, as suggested by Forbes et al. [23], and this yields the further system of differential equations

$$\sum_{n=1}^N S^{(1)}_{\ell n}(t)B_n'(t) + \sum_{n=1}^N S^{(2)}_{\ell n}(t)C_n'(t) + \left[\frac{1}{4\pi A^2(t)} + H_0'(t)\right]T_{\ell 0} + \sum_{n=1}^N T_{\ell n}H_n'(t) = 0, \quad \ell = 1, 2, \ldots, N, \tag{2.27}$$

involving the Fourier coefficients. The additional intermediate functions

$$T_{\ell n}(t) = \int_0^\pi R(W_2 - W_1)P_\ell'(\cos\phi)P_n(\cos\phi)\sin^2\phi\, d\phi \tag{2.28}$$

have been defined for convenience of notation.

The dynamic condition (2.12) is similarly subjected to Fourier–Legendre decomposition. The contribution from the zeroth-order Fourier modes is obtained by multiplying by $\sin\phi$ and integrating, which results in

$$D\sum_{n=1}^N K^{(2)}_{0n}C_n'(t) - 2B_0'(t) - \sum_{n=1}^N K^{(1)}_{0n}B_n'(t) + \frac{1}{2}DJ_0^{(2)} - \frac{1}{2}J_0^{(1)} - \frac{(D-1)Y_0}{F^2} = (D-1)\left[\frac{1}{(4\pi)^2A^4(t)} - \frac{2}{F^2A(t)}\right]. \tag{2.29}$$

https://doi.org/10.1017/S1446181112000090 Published online by Cambridge University Press

The higher-order Fourier modes result from multiplying equation (2.12) by the basis functions $P_\ell(\cos\phi)\sin\phi$ and integrating. This gives the further system of differential equations

$$D\sum_{n=1}^{N} K_{\ell n}^{(2)} C_n'(t) - \sum_{n=1}^{N} K_{\ell n}^{(1)} B_n'(t) + \frac{1}{2} D J_\ell^{(2)} - \frac{1}{2} J_\ell^{(1)} - \frac{(D-1)Y_\ell}{F^2} = 0. \tag{2.30}$$

In these expressions, it has proven convenient to define the intermediate functions

$$K_{\ell n}^{(1)}(t) = \int_0^\pi R^n P_\ell(\cos\phi) P_n(\cos\phi)\sin\phi\, d\phi, \tag{2.31}$$

$$K_{\ell n}^{(2)}(t) = \int_0^\pi R^{-n-1} P_\ell(\cos\phi) P_n(\cos\phi)\sin\phi\, d\phi, \tag{2.32}$$

$$J_\ell^{(1)}(t) = \int_0^\pi (U_1^2 + W_1^2) P_\ell(\cos\phi)\sin\phi\, d\phi, \tag{2.33}$$

$$J_\ell^{(2)}(t) = \int_0^\pi (U_2^2 + W_2^2) P_\ell(\cos\phi)\sin\phi\, d\phi, \tag{2.34}$$

$$Y_\ell(t) = \int_0^\pi \frac{1}{R} P_\ell(\cos\phi)\sin\phi\, d\phi, \tag{2.35}$$

for $n = 1, 2, \ldots, N$ and $\ell = 0, 1, 2, \ldots, N$.

These differential equations for the evolution of the Fourier coefficients in time are now integrated numerically. The zeroth-order dynamical condition (2.29) is essentially just a differential equation for the quantity $B_0(t)$. However, since this can be ignored in equations (2.13) and (2.14) with no penalty to the velocity components in fluid 1, both B_0 and the condition (2.29) are disregarded in the numerical solution. This then leaves the system of $3N + 1$ differential equations (2.19), (2.21), (2.27) and (2.30). This matrix system of ordinary differential equations is integrated forward in time using the classical fourth-order Runge–Kutta method described by Atkinson [4, p. 371]. The intermediate quantities in equations (2.20), (2.22), (2.23), (2.26), (2.28) and (2.31)–(2.35) all involve periodic integrands, and are evaluated using the composite trapezoidal rule, which is exponentially accurate in these cases [4, p. 253]. Highly converged results are obtained here using up to $N = 45$ Fourier modes and with 401 spatial points in the angle ϕ for the numerical evaluation of the integrals.

The initial conditions for the flow are assumed to be that the interface is spherical, but that the velocity is subject to a small perturbation. Thus

$$H_0(0) = 0 \quad \text{and} \quad H_n(0) = 0, \quad n = 1, 2, \ldots, N, \tag{2.36}$$

so that $R(\phi, 0) = 1$ from equations (2.15) and (2.3). If a perturbation at the Kth Fourier mode is desired at time $t = 0$, then this may be achieved by taking $B_n(0) = 0$

https://doi.org/10.1017/S1446181112000090 Published online by Cambridge University Press

and $C_n(0) = 0$ in equations (2.13) and (2.14), except for

$$B_K(0) = \frac{\epsilon}{K} \quad \text{and} \quad C_K(0) = -\frac{\epsilon}{K+1}, \tag{2.37}$$

in which ϵ is a small parameter related to the amplitude of the initial perturbation.

In order to speed up the numerical algorithm, it has been found useful to cache the functions $P_n(\cos\phi)$ and the derivatives $P_n'(\cos\phi)$. These are computed from the three-term recurrence relations

$$\begin{aligned}
&P_0(\cos\phi) = 1, \quad P_1(\cos\phi) = \cos\phi, \quad P_1'(\cos\phi) = 1,\\
&P_{n+1}(\cos\phi) = \left(\frac{2n+1}{n+1}\right)\cos\phi P_n(\cos\phi) - \left(\frac{n}{n+1}\right)P_{n-1}(\cos\phi),\\
&P_{n+1}'(\cos\phi) = \cos\phi P_n'(\cos\phi) + (n+1)P_n(\cos\phi).
\end{aligned}$$

These formulae may be derived from identities given by Abramowitz and Stegun [1].

3. The linearized inviscid model

If the amplitude ϵ of the velocity perturbation in the initial conditions (2.37) is small, it is possible to construct a linearized problem, in which the interface shape is assumed to represent only a small change to the spherical surface $r = A(t)$ in equation (2.3). The two velocity potentials and the interface shape are expressed in terms of the regular expansions

$$\Phi_1(r,\phi,t) = -\frac{1}{4\pi r} + \epsilon\Phi_{11}(r,\phi,t) + O(\epsilon^2), \tag{3.1}$$

$$\Phi_2(r,\phi,t) = -\frac{1}{4\pi r} + \epsilon\Phi_{21}(r,\phi,t) + O(\epsilon^2), \tag{3.2}$$

$$R(\phi,t) = A(t) + \epsilon R_1(\phi,t) + O(\epsilon^2). \tag{3.3}$$

These expressions are substituted into the governing equations and terms are retained to the first order in powers of the small parameter ϵ.

It is found that the perturbation potential Φ_{11} in (3.1) satisfies Laplace's equation (2.5) within the linearized zone $r < A(t)$, and the potential Φ_{21} in (3.2) similarly satisfies this equation in $r > A(t)$. The two kinematic conditions (2.9) take the linearized form

$$\frac{\partial\Phi_{j1}}{\partial r} = \frac{\partial R_1}{\partial t} + \frac{R_1}{2\pi A^3(t)}, \quad j = 1, 2, \quad \text{on } r = A(t), \tag{3.4}$$

and the dynamic condition (2.12) linearizes to

$$\begin{aligned}
&D\frac{\partial\Phi_{21}}{\partial t} - \frac{\partial\Phi_{11}}{\partial t} + \frac{D}{4\pi A^2(t)}\frac{\partial\Phi_{21}}{\partial r} - \frac{1}{4\pi A^2(t)}\frac{\partial\Phi_{11}}{\partial r}\\
&\quad - \frac{2(D-1)R_1}{(4\pi)^2A^5(t)} + \frac{(D-1)R_1}{F^2A^2(t)} = 0 \quad \text{on } r = A(t).
\end{aligned} \tag{3.5}$$

https://doi.org/10.1017/S1446181112000090 Published online by Cambridge University Press

If a perturbation at the Kth Fourier mode is assumed, as in the initial conditions (2.37), then the solution for the linearized potentials is

$$\Phi_{11}(r, \phi, t) = B_K(t) r^K P_K(\cos\phi), \quad r < A(t), \tag{3.6}$$

$$\Phi_{21}(r, \phi, t) = C_K(t) r^{-K-1} P_K(\cos\phi), \quad r > A(t), \tag{3.7}$$

which follows directly from the more general representation given in equations (2.13) and (2.14).

The two linearized kinematic conditions in (3.4) are subtracted and the potentials in (3.6) and (3.7) are substituted into the resulting equation. This shows that the coefficients are related according to the formula

$$C_K(t) = -\left(\frac{K}{K+1}\right) B_K(t) A^{2K+1}(t). \tag{3.8}$$

It follows from the linearized dynamic condition (3.5) that the perturbed interface shape has the form

$$R_1(\phi, t) = -\frac{[(D+1)K+1]}{(D-1)(K+1)} G_1(t) P_K(\cos\phi), \tag{3.9}$$

in which

$$G_1(t) = \frac{B_K'(t) A^{K+5}(t) + (K/(4\pi)) B_K(t) A^{K+2}(t)}{2/(4\pi)^2 - A^3(t)/F^2},$$

after use is made of relation (3.8). Finally, equation (3.9) is substituted into the first of the linearized kinematic conditions in (3.4), and after some algebra an ordinary differential equation of the form

$$A^{K+5}(t) \frac{d^2 B_K}{dt^2} + F_1(t) \frac{dB_K}{dt} + F_0(t) B_K = 0 \tag{3.10}$$

is obtained for the coefficient $B_K(t)$. The intermediate functions appearing in this expression are defined to be

$$F_1(t) = \frac{(2K+7)}{4\pi} A^{K+2}(t) + \frac{3}{4\pi F^2} \frac{A^{K+5}(t)}{[2/(4\pi)^2 - A^3(t)/F^2]},$$

$$F_0(t) = \frac{(D-1)(K+1)}{[(D+1)K+1]} \left[\frac{2K}{(4\pi)^2} A^{K-1}(t) - \frac{K}{F^2} A^{K+2}(t) \right] + \frac{K(K+4)}{(4\pi)^2} A^{K-1}(t) + \frac{3K}{(4\pi)^2 F^2} \frac{A^{K+2}(t)}{[2/(4\pi)^2 - A^3(t)/F^2]}.$$

This differential equation, although linear, does not have a straightforward solution in closed form.

https://doi.org/10.1017/S1446181112000090 Published online by Cambridge University Press

In the limit that the inwardly directed acceleration due to gravity is zero, the Froude number $F \to \infty$, as is evident from the definition (2.4). In this special case, the perturbed interface shape function R_1 takes the form

$$R_1(\phi, t) \to -\frac{[(D+1)K+1]}{(D-1)(K+1)}\frac{(4\pi)^2}{2}\eta_K(t)P_K(\cos\phi),$$

in which it is appropriate to define

$$\eta_K(t) = B_K'(t)A^{K+5}(t) + \frac{K}{4\pi}B_K(t)A^{K+2}(t). \tag{3.11}$$

Now it is possible to eliminate B_K in favour of the amplitude variable η_K in (3.11), and after some algebra the differential equation (3.10) becomes

$$\eta_K''(t) + 3\frac{A'(t)}{A(t)}\eta_K'(t) - \frac{A''(t)}{A(t)}\eta_K(t)\left[\frac{(D-1)K(K+1)}{(D+1)K+1} - 2\right] = 0 \tag{3.12}$$

in the variable η_K. The differential equation (3.12) is identical to that derived by Mikaelian [39, equations (1c) and (2)].

It is possible to obtain the solution of the differential equation (3.10) in the zero-gravity case $F \to \infty$ by regarding the unperturbed radius A in equation (2.3) as the independent variable, rather than time t. In the absence of gravity, the governing differential equation becomes

$$A^2\frac{d^2B_K}{dA^2} + A\frac{dB_K}{dA}(2K+5) + KB_K\left[\frac{2(D-1)(K+1)}{[(D+1)K+1]} + K + 4\right] = 0. \tag{3.13}$$

Equation (3.13) is of Euler–Cauchy type and, subject to the initial conditions (2.36) and (2.37), gives the solution

$$B_K(t) = \left(\frac{2+\beta}{2\beta K}\right)A^{-K-2+\beta} - \left(\frac{2-\beta}{2\beta K}\right)A^{-K-2-\beta}$$

for the Fourier coefficient B_K. The linearized solution for the perturbed interface shape in (3.3) then becomes

$$R_1(\phi, t) = \frac{2\pi}{\beta}[A^\beta - A^{-\beta}]P_K(\cos\phi). \tag{3.14}$$

The constant β in the solution (3.14) is determined from the expression

$$\beta^2 = \frac{4(D+1)K + 4 - 2K(K+1)(D-1)}{(D+1)K+1}. \tag{3.15}$$

Perturbations R_1 to the expanding bubble of fluid 1 will grow unstably if the constant β in equation (3.15) is real. This is the case whenever $0 < D < 1$. For $D > 1$, this also gives rise to the condition

$$D < \frac{(K+1)(K+2)}{K(K-1)}. \tag{3.16}$$

https://doi.org/10.1017/S1446181112000090 Published online by Cambridge University Press

Thus the lowest Fourier mode $K = 1$ is always unstable for any density ratio D, as may be confirmed directly from equation (3.15), and so grows exponentially with time. The bipolar mode $K = 2$ is unstable for any density ratio $D < 6$, as indicated by inequality (3.16). This is possibly a case of some interest in astrophysical applications, particularly in the context of star formation. As indicated by Stahler and Palla [49], bipolar flow is often observed in outflow from young stars, although magnetic fields may perhaps play a strong role in that situation and are ignored in the present study. Inequality (3.16) shows that the *lowest* Fourier modes are actually the most unstable, and as $K \to \infty$ this condition in fact suggests instability only when $D < 1$. This indicates that higher modes are less affected by the Rayleigh–Taylor instability when $D > 1$; rather, it is the curved geometry of the spherical surface that is the driving mechanism for growth in these higher modes. This phenomenon is the Bell–Plesset effect, and is discussed by Epstein [18], who points out that it can act as a further destabilizing influence on the usual Rayleigh–Taylor instability.

An essentially similar conclusion can be derived from the linearized equation (3.10) for the full system, in spite of the fact that there is no closed-form solution to it in general. When the mode number K is very large, the differential equation becomes asymptotically

$$A^6(t)\frac{d^2B_K}{dt^2} + \frac{K}{2\pi}A^3(t)\frac{dB_K}{dt} + \frac{K^2}{(4\pi)^2}B_K = 0.$$

When the unperturbed sphere radius $A(t)$ is again regarded as the independent variable rather than time t, this equation takes the form

$$A^2\frac{d^2B_K}{dA^2} + 2(K-1)A\frac{dB_K}{dA} + K^2B_K = 0,$$

following similar developments to those used in obtaining equation (3.13). This is again a differential equation of Euler–Cauchy type, and for large K it takes solutions of the asymptotic form

$$B_K \sim A^\lambda \quad \text{with } \lambda \sim -K \pm i\sqrt{3K}. \tag{3.17}$$

The result (3.17) again confirms that higher-order modes are the most stable, at least when $D > 1$, so that they are most strongly influenced by Bell–Plesset effects rather than directly by the Rayleigh–Taylor instability alone.

4. The Boussinesq model for viscous flow

The inclusion of viscous effects in this model requires the solution of the usual Navier–Stokes equations in both fluids, subject to the conditions of continuity of the normal and tangential components of the stress tensor at the interface, as given by Batchelor [9, p. 150]. This is a difficult task, and is circumvented here by instead adopting an approximate Boussinesq model for viscosity, following the approach taken by Farrow and Hocking [19], who used it to study viscous effects on the withdrawal

https://doi.org/10.1017/S1446181112000090 Published online by Cambridge University Press

of fluid from a tank. In this approach, the two distinct and immiscible fluids 1 and 2 in Figure 1 are replaced with a single (miscible) fluid that is regarded as weakly compressible, so that the interface is approximated by a narrow region in which the density changes rapidly but smoothly. As the outflow from a point source is irrotational, the radial and axial velocity components u and w can still be obtained from (2.7), and represent an exact solution to the Navier–Stokes equations of viscous flow.

Dimensionless variables are defined as previously in Section 2, such that the reference length is the initial radius a of the bubble and a^3/m is the reference time, in which m denotes the strength of the sink (volume per unit time) in dimensional units. The density is written in the dimensionless form $\rho(r,\phi,t) = 1+\bar{\rho}$ and it is understood that the quantity $\bar{\rho}(r,\phi,t)$ is small relative to unity. The full continuity equation expressing conservation of mass (for a compressible fluid) is "split" into an incompressible part

$$\frac{1}{r^2}\frac{\partial(r^2u)}{\partial r} + \frac{1}{r\sin\phi}\frac{\partial(\sin\phi w)}{\partial\phi} = 0 \tag{4.1}$$

involving the velocity components u and w, and a weakly compressible part

$$\frac{\partial\bar{\rho}}{\partial t} + u\frac{\partial\bar{\rho}}{\partial r} + \frac{w}{r}\frac{\partial\bar{\rho}}{\partial\phi} = \sigma\left[\frac{\partial^2\bar{\rho}}{\partial r^2} + \frac{2}{r}\frac{\partial\bar{\rho}}{\partial r} + \frac{\cot\phi}{r^2}\frac{\partial\bar{\rho}}{\partial\phi} + \frac{1}{r^2}\frac{\partial^2\bar{\rho}}{\partial\phi^2}\right] \tag{4.2}$$

for the perturbed density function. Here σ is a density diffusion coefficient related to a Prandtl number associated with the stratification (see the paper of Farrow and Hocking [19]) and made dimensionless by reference to the quantity m/a.

As in the papers of Forbes [22] and Forbes and Hocking [24], it is convenient to adopt a vorticity streamfunction approach to these equations, rather than the primitive variables system used by Farrow and Hocking [19]. Thus equation (4.1) is satisfied identically by a streamfunction $\Psi(r,\phi,t)$ from which the velocity components u and w are obtained by means of the equations

$$u = \frac{1}{r\sin\phi}\frac{\partial(\sin\phi\Psi)}{\partial\phi}, \qquad w = -\frac{1}{r}\frac{\partial(r\Psi)}{\partial r}. \tag{4.3}$$

The vorticity is defined in the usual way as the vector curl of the fluid velocity vector, and in these spherical coordinates it has the form $\zeta\mathbf{e}_\theta$ of a vector pointing in the purely azimuthal $\mathbf{e}_\theta$ direction, with the single component

$$\zeta = -\left[\frac{\partial^2\Psi}{\partial r^2} + \frac{2}{r}\frac{\partial\Psi}{\partial r} + \frac{\cot\phi}{r^2}\frac{\partial\Psi}{\partial\phi} + \frac{1}{r^2}\frac{\partial^2\Psi}{\partial\phi^2} - \frac{\Psi}{r^2\sin^2\phi}\right]. \tag{4.4}$$

By taking the curl of the viscous Navier–Stokes equations, with the Boussinesq approximation $\rho = 1+\bar{\rho}$, a transport equation is derived for the vorticity ζ in

https://doi.org/10.1017/S1446181112000090 Published online by Cambridge University Press

equation (4.4). This takes the form

$$\frac{\partial\zeta}{\partial t}+u\frac{\partial\zeta}{\partial r}+\frac{w}{r}\frac{\partial\zeta}{\partial\phi}-\frac{\zeta}{r}(u+w\cot\phi)$$
$$=\frac{1}{F^2r^3}\frac{\partial\bar{\rho}}{\partial\phi}+\frac{1}{R_e}\left[\frac{\partial^2\zeta}{\partial r^2}+\frac{2}{r}\frac{\partial\zeta}{\partial r}+\frac{\cot\phi}{r^2}\frac{\partial\zeta}{\partial\phi}+\frac{1}{r^2}\frac{\partial^2\zeta}{\partial\phi^2}-\frac{\zeta}{r^2\sin^2\phi}\right]. \tag{4.5}$$

The constant R_e in this expression is the viscous Reynolds number. It is defined from the dimensional quantities as $R_e = m/(\nu a)$, in which ν represents the dynamic viscosity of the fluid. Equation (4.5) is of a similar form to the usual vorticity equation given by Batchelor [9, p. 267].

Near the source, the streamfunction behaves as

$$\Psi\to-\frac{\cot\phi}{4\pi r}\quad\text{as } r\to 0, \tag{4.6}$$

and in fact this is an exact solution to the system (4.2)–(4.5) if $\bar{\rho}$ is constant, since it represents irrotational outflow from the source. For computational purposes, uniform outflow is also imposed at some "artificial" boundary $r=\beta$, chosen to be sufficiently far from the source as to have only a minor effect on the details of the outflow. This is achieved here by imposing

$$\Psi(\beta,\phi,t)=-\frac{\cot\phi}{4\pi\beta},\quad \zeta(\beta,\phi,t)=0\quad\text{at } r=\beta. \tag{4.7}$$

The second condition in (4.7) is equivalent to allowing slip on this artificial boundary, consistently with the Boussinesq viscous approximation employed by Farrow and Hocking [19].

A spectral solution is now sought to this nonlinear weakly viscous system. A representation must be chosen for the streamfunction, such that the outflow conditions (4.6) and (4.7) are satisfied identically, but which is consistent with the developments in Section 2 in the purely irrotational case. Therefore, it is appropriate to choose

$$\Psi(r,\phi,t)=-\frac{\cot\phi}{4\pi r}+\sum_{m=1}^{M}\sum_{n=1}^{N}B_{mn}(t)\frac{J_{n+1/2}(\alpha_{n,m}r)}{\sqrt{r}}P_n'(\cos\phi)\sin\phi. \tag{4.8}$$

In this expression, P_n are the Legendre polynomials, as in Section 2, and $J_{n+1/2}$ are the Bessel functions of first kind, of half-fractional order. It is convenient to define the constants

$$\alpha_{n,m}=\frac{j_{n+1/2,m}}{\beta}, \tag{4.9}$$

in which the symbol $j_{\nu,s}$ denotes the sth zero of the Bessel function of order ν, consistently with the notation of Abramowitz and Stegun [1, p. 370].

https://doi.org/10.1017/S1446181112000090 Published online by Cambridge University Press

The equations in (4.3) combined with the representation (4.8) show that the radial and axial velocity components may be expressed in the forms

$$u(r,\phi,t) = \frac{1}{4\pi r^2} + \sum_{m=1}^{M}\sum_{n=1}^{N} n(n+1)B_{mn}(t)\frac{J_{n+1/2}(\alpha_{n,m}r)}{r^{3/2}}P_n(\cos\phi) \tag{4.10}$$

and

$$w(r,\phi,t) = -\sum_{m=1}^{M}\sum_{n=1}^{N} B_{mn}(t)\Big[\frac{1}{2}r^{-3/2}J_{n+1/2}(\alpha_{n,m}r) + \alpha_{n,m}r^{-1/2}J'_{n+1/2}(\alpha_{n,m}r)\Big]P'_n(\cos\phi)\sin\phi.$$

Finally, the vorticity is obtained from the definition (4.4) as the expression

$$\zeta(r,\phi,t) = \sum_{m=1}^{M}\sum_{n=1}^{N} A_{mn}(t)\frac{J_{n+1/2}(\alpha_{n,m}r)}{\sqrt{r}}P'_n(\cos\phi)\sin\phi,$$

in which the new coefficients are defined to be

$$A_{mn}(t) = (\alpha_{n,m})^2 B_{mn}(t),$$

with $\alpha_{n,m}$ given in equation (4.9). As yet, these coefficients A_{mn} and B_{mn} are unknown functions of time.

After a careful analysis of the vorticity equation (4.5), it is evident that the appropriate representation for the perturbed density must be

$$\bar{\rho}(r,\phi,t) = (D-1)\Big(\frac{r}{\beta}\Big)^3 + \sum_{m=1}^{M} C_{m0}(t)\sin\Big(\frac{m\pi r^3}{\beta^3}\Big) + \sum_{m=1}^{M}\sum_{n=1}^{N} C_{mn}(t)r^{5/2}J_{n+1/2}(\alpha_{n,m}r)P_n(\cos\phi). \tag{4.11}$$

The additional coefficients C_{mn} in equation (4.11) are also unknown at this stage.

The governing equations are now spectrally decomposed, using the orthogonality relations

$$\int_0^{\pi} P_n(\cos\phi)P_\ell(\cos\phi)\sin\phi\,d\phi = \begin{cases} 0 & \text{if } \ell \neq n \\ 2/(2n+1) & \text{if } \ell = n \end{cases} \tag{4.12}$$

for the Legendre polynomials, and

$$\int_0^{\beta} rJ_{\ell+1/2}(\alpha_{\ell,m}r)J_{\ell+1/2}(\alpha_{\ell,k}r)\,dr = \begin{cases} 0 & \text{if } m \neq k \\ (\beta^2/2)J^2_{\ell+3/2}(\alpha_{\ell,k}\beta) & \text{if } m = k \end{cases} \tag{4.13}$$

https://doi.org/10.1017/S1446181112000090 Published online by Cambridge University Press

for the first-kind Bessel functions. These results may be derived from well-known identities given in Gradshteyn and Ryzhik [26] (p. 782, formula 7.221.1 and p. 658, formula 6.521.1, respectively).

The density equation (4.2) is first multiplied by $\sin\phi$ and integrated, making use of (4.12). The resulting expression is then further multiplied by $r^2\sin(k\pi r^3/\beta^3)$ and integrated with respect to r. This gives a system of ordinary differential equations for the zeroth-order coefficients C_{m0}, presented in Appendix A as (A.1). The Fourier modes for the general ℓth Fourier mode in ϕ are similarly derived by first multiplying equation (4.2) by $P_\ell(\cos\phi)\sin\phi$ and integrating over ϕ, then multiplying by $r^{-3/2}J_{\ell+1/2}(\alpha_{\ell,k}r)$ and integrating over r. This gives a further system of MN differential equations, presented in Appendix A as (A.2).

A similar Fourier decomposition process is applied to the vorticity equation (4.5). This expression is first multiplied by $P'_\ell(\cos\phi)\sin^2\phi$ and integrated over the interval $0<\phi<\pi$. It is necessary to make use of the further orthogonality relation

$$\int_0^\pi P'_n(\cos\phi)P'_\ell(\cos\phi)\sin^3\phi\,d\phi=\begin{cases}0 & \text{if } \ell\neq n\\ 2n(n+1)/(2n+1) & \text{if } \ell=n\end{cases} \tag{4.14}$$

for the derivatives of Legendre polynomials. The result (4.14) may be derived from an identity given by Abramowitz and Stegun [1, p. 338, formula 8.14.11]. The resulting equation is now further multiplied by $r^{3/2}J_{\ell+1/2}(\alpha_{\ell,k}r)$ and integrated over r, making use of the identity (4.13). After some algebra, a system of MN ordinary differential equations is obtained for the Fourier coefficients $A_{k\ell}$, and these equations are also given in Appendix A as the system (A.3), for completeness.

It remains to specify appropriate initial conditions for the flow. For comparison with the inviscid solution in Section 2, conditions are chosen so as to imitate (2.36) and (2.37) as closely as possible. The initial density profile is therefore chosen to be

$$\bar\rho(r,\phi,0)=\begin{cases}0 & \text{if } 0<r<1\\ D-1 & \text{if } 1<r<\beta,\end{cases} \tag{4.15}$$

corresponding to an effective interface at initial radius $r=1$. The representation (4.11) is made equal to the profile (4.15) at $t=0$ and Fourier analysed. This shows that the appropriate choice for the coefficients in expression (4.11) is

$$C_{k0}(0)=\frac{2(D-1)}{k\pi}\cos(k\pi/\beta^3), \tag{4.16}$$

$$C_{k\ell}(0)=0,\quad k=1,2,\ldots,M,\ \ell=1,2,\ldots,N. \tag{4.17}$$

In order to achieve an initial velocity perturbation at the Kth mode, mimicking (2.37) for the inviscid solution, it is appropriate to impose the initial radial velocity

$$u(r,\phi,0)=\frac{1}{4\pi r^2}+\begin{cases}\epsilon r^{K-1}P_K(\cos\phi) & \text{if } 0<r<1\\ \epsilon r^{-K-2}P_K(\cos\phi) & \text{if } 1<r<\beta.\end{cases} \tag{4.18}$$

https://doi.org/10.1017/S1446181112000090 Published online by Cambridge University Press

This is now compared with the representation (4.10) at the initial time, and spectrally decomposed to give the coefficients. It is found that $A_{mn}(0) = 0$ in general, except for the Kth mode, in which case

$$A_{mK}(0) = \frac{2\epsilon\alpha_{K,m}}{K(K+1)\beta^2 J^2_{K+3/2}(\alpha_{K,m}\beta)}\left[\frac{(2K+1)}{\alpha_{K,m}}J_{K+1/2}(\alpha_{K,m}) - \frac{J_{K-1/2}(\alpha_{K,m}\beta)}{\beta^{K-1/2}}\right]. \quad (4.19)$$

The constant ϵ is a small parameter related to the amplitude of the initial perturbation, precisely as in Section 2.

The time evolution of the viscous Boussinesq outflow at the Kth mode is thus determined by solving the system of $M(2N+1)$ ordinary differential equations (A.1)–(A.3) for the Fourier coefficients, subject to the initial conditions (4.16), (4.17) and (4.19). This has been done by a variety of integration schemes, but in order to reduce computer run time and to improve accuracy, a fourth-/fifth-order adaptive Runge–Kutta–Fehlberg algorithm bas been used for the results presented in this paper (see the book by Atkinson [4]). The integrals with respect to the axial angle ϕ in these differential equations are evaluated numerically using the composite trapezoidal rule, which is extremely accurate for periodic integrands, as indicated by Atkinson [4, p. 253]. The integrations with respect to the radial coordinate r are performed to a high degree of accuracy using the Gauss–Legendre routine provided by von Winckel [52]. The Legendre polynomials and Bessel functions are computed only once and then cached in computer memory, as this greatly reduces the run time of the solution algorithm. Converged results are obtained with $M = N = 25$ coefficients and 81 numerical integration points in both r and ϕ, and the time steps are chosen adaptively by the integration algorithm.

5. Presentation of results

A large number of solutions have been computed with the techniques outlined in Sections 2 and 4, for a variety of different parameter values. In this paper, however, a sample cross-section of results is presented, which is nevertheless representative of the solution behaviour in general. The density ratio is set at the value $D = 1.05$, which is typical for a fresh-water–salt-water interface, for example, and for simplicity the Froude number is fixed at $F = 1$. The amplitude of the initial velocity perturbation is taken to be $\epsilon = 0.03$. For the viscous results, it is convenient to take the density diffusion parameter and the Reynolds number to have the values $\sigma = 10^{-4}$ and $\mathrm{Re} = 250$, respectively, although the solutions are not qualitatively affected by this choice.

The evolution of an inviscid interface, calculated using the methods of Section 2, is shown in Figure 2. This is a solution obtained at the second mode $K = 2$, representing an outflow that is initially bipolar in the presence of a gravitational field. Results are presented at the five times $t = 1, 2, 3, 4, 5$, and were obtained with $N = 45$ Fourier–Legendre modes, using 401 points along the interface. Figure 2(a) shows the actual interface shape at the different times; the scale on both axes is the same, so that the profiles are as they would actually appear in cross-section on the plane $y = 0$. Since

https://doi.org/10.1017/S1446181112000090 Published online by Cambridge University Press

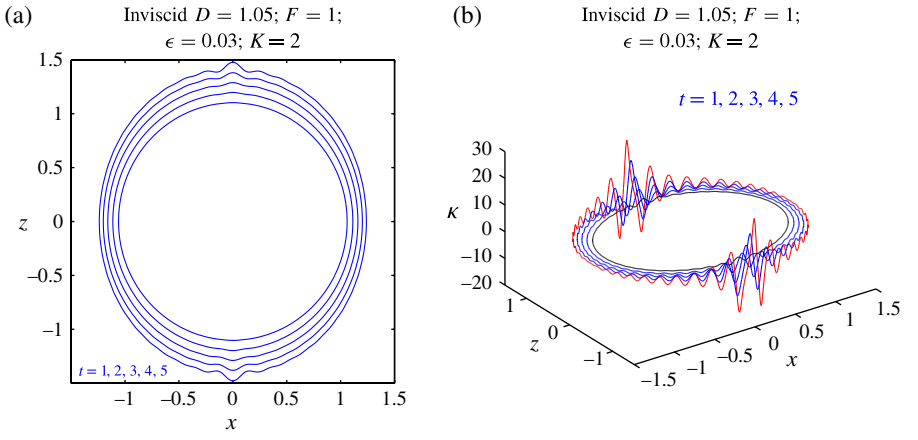

FIGURE 2. The inviscid solution at five different times $t = 1, 2, 3, 4, 5$, computed with parameter values $D = 1.05$, $F = 1$, $\epsilon = 0.03$, for the second mode $K = 2$. Results are shown for (a) the interface shape and (b) the curvature. The scale in (a) is the same on both axes.

axial symmetry is assumed in this paper, the interfacial surfaces at the different times can be obtained by rotating the shapes in Figure 2(a) about the z-axis.

From Figure 2(a), it is evident that although the interface begins as a sphere at time $t = 0$, it evolves into a shape with pointed lobes at the two poles as the outflow progresses. This continues up until about time $t = 7$, after which the numerical algorithm of Section 2 fails. Similar behaviour is known to occur in the planar and cylindrical Rayleigh–Taylor problems, and has been discussed by Forbes [21, 22]. It is associated in both those geometries with the formation of a curvature singularity at the interface, within finite time; this effect has been studied extensively in the planar case by Moore [40], Baker et al. [6] and Cowley et al. [15]. The pointed regions in Figure 2(a) on the interface at the two poles suggest that a similar phenomenon is likely in this axially symmetric geometry also.

For a parametrically defined space curve $\mathbf{r}(s)$ with parameter s, the curvature may be obtained from the formula

$$\kappa = \frac{\sqrt{(\mathbf{r}' \cdot \mathbf{r}')(\mathbf{r}'' \cdot \mathbf{r}'') - (\mathbf{r}' \cdot \mathbf{r}'')^2}}{(\mathbf{r}' \cdot \mathbf{r}')^{3/2}}, \tag{5.1}$$

in which primes denote derivatives of the indicated vector with respect to s. This result may be obtained from the book by Kreyszig [30, p. 400]. For the spherical coordinate system in (2.1), in which the inviscid interface is written in the form $r = R(\phi, t)$, the curvature (5.1) may be shown to be given by the expression

$$\kappa = \frac{R^2 + 2R_\phi^2 - RR_{\phi\phi}}{(R^2 + R_\phi^2)^{3/2}}, \tag{5.2}$$

https://doi.org/10.1017/S1446181112000090 Published online by Cambridge University Press

and this is evaluated directly from the spectral representation (2.15), using exact differentiation.

Figure 2(b) shows the curvature computed from equation (5.2), for the same five times as in Figure 2(a). At the initial time $t = 0$, the interface is simply a sphere of unit radius, and so it has constant curvature $\kappa = 1$. This is also approximately true at the earliest time $t = 1$ shown in Figure 2(b), as may be seen from the diagram. As time progresses, however, large spikes in curvature appear at the two poles, and these are evident in the figure. This is consistent with the suggestion of a finite-time curvature singularity at about $t = 7$.

Solutions for this same case $K = 2$ have been computed for a Boussinesq viscous fluid using the method outlined in Section 4. In this method, it is necessary to impose an artificial boundary at $r = \beta$, as in (4.7), and here $\beta = 5$ has been found to give reliable solutions. It is found that, in the early stages of the evolution of the flow, there is close agreement between the predictions of this viscous approach with the interface computed from the inviscid theory, as is discussed more fully later.

Figure 3(a) shows contours of the density perturbation $\bar{\rho}$ at three times $t = 2$, 3 and 4. Necessarily, the scale on the horizontal and vertical axes is not the same, but these three diagrams are sufficient to reveal an interesting effect. For this second-mode solution ($K = 2$), the outflow is bipolar at early times, and is very similar to the results presented in Figure 2(a). The solution at $t = 3$ even shows the similar peaked structure at the two poles. However, by $t = 4$ the solution starts to lose its bipolar symmetry and instead develops a stronger jet at the bottom of the picture than the corresponding jet at the top. This has been checked carefully and is a genuine feature of the solution rather than a mere numerical artifact, and more detail is given in regard to this issue in Section 6. It is simply observed here that, since the gravitational body force is purely radial and directed inward toward the origin, there is no preferred "top" or "bottom" in these figures; thus, changes to numerical features (such as the number of coefficients used) may change whether the larger jet appears at the top or the bottom of the diagrams, but the solution is otherwise unchanged under a simple rotation through 180°. Evidently, the mode-one configuration is the preferred outflow type, so that different initial conditions eventually give rise to this configuration.

This is investigated further in Figure 3(b), where contours of the vorticity function ζ are shown for this solution at the same three times. In the inviscid solution of Section 2, this function is identically zero over the whole region, but now the introduction of viscosity in Figure 3 provides a mechanism for vorticity to be produced. Nevertheless, the vorticity is zero over almost all of the solution domain, which certainly justifies the approximation in (4.7) that vorticity could be set approximately to zero on the edge $r = \beta$ of the computational domain. At the early times $t = 2$ and $t = 3$, the vorticity retains a bipolar form, being antisymmetric about the plane $z = 0$. However, by time $t = 4$ the vorticity is clearly concentrated either side of the narrow jet escaping toward the bottom of the picture.

As a further aid to flow visualization, the instantaneous streamlines for this same flow are presented in Figure 3(c). From Batchelor [9], streamlines are curves in

https://doi.org/10.1017/S1446181112000090 Published online by Cambridge University Press

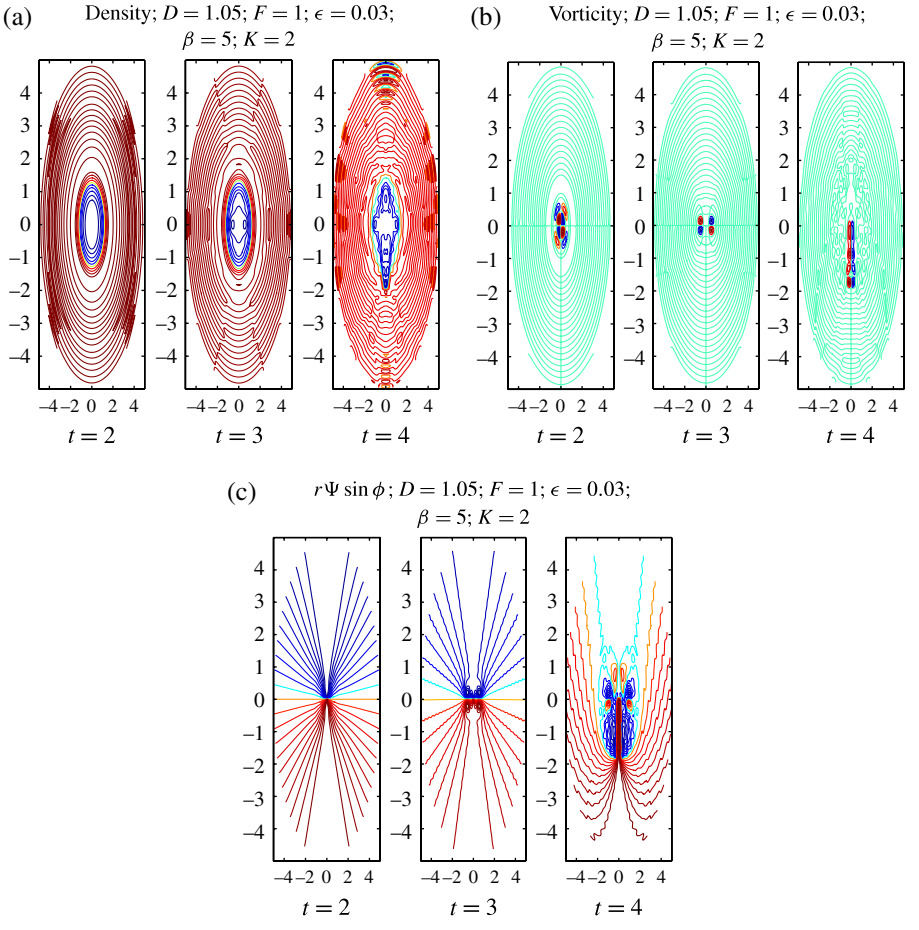

FIGURE 3. The viscous solution at the three times $t = 2, 3, 4$ for the case $D = 1.05$, $F = 1$, $\epsilon = 0.03$, $\beta = 5$, for the second mode $K = 2$. Solution contours are shown for (a) the density, (b) the vorticity and (c) a variable related to the location of the streamlines.

the fluid for which the tangent is parallel to the velocity vector; from the streamline equations in the present spherical coordinates (2.1) it is straightforward to show that, at least in steady flow, the quantity $r\Psi \sin\phi$ is constant along streamlines. Accordingly, this has been calculated for these viscous flows, based on the representation in equation (4.8), and contours drawn at the three times shown. At the early time $t = 2$, the streamlines are approximately just straight lines emanating from the origin, as is to be expected for purely radial outflow from a point source. At the next time $t = 3$, this largely continues to be the case, although viscous entrainment near the source has created small recirculating regions near the origin, and these are consistent with the vorticity patterns at this time shown in Figure 3(b). However, the bipolar nature of the flow is still in evidence, as the streamline pattern remains symmetric about the

https://doi.org/10.1017/S1446181112000090 Published online by Cambridge University Press

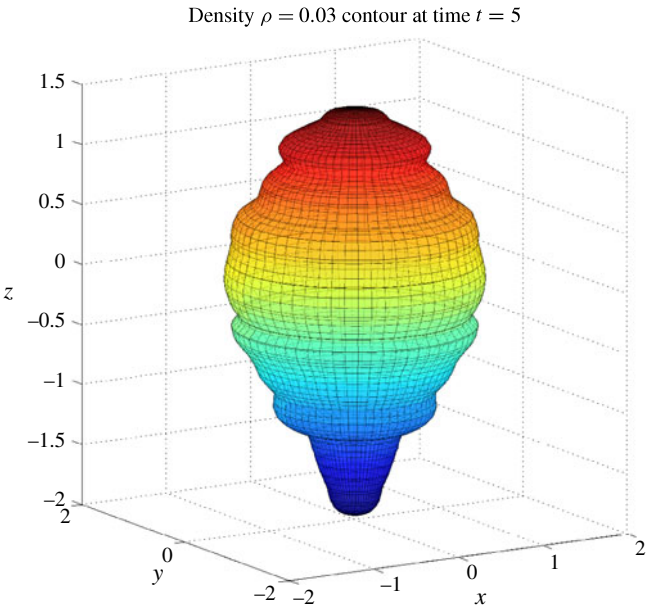

FIGURE 4. The axi-symmetric surface formed by the density contour $\bar{\rho} = 0.03$ in the viscous solution at time $t = 5$, for the case $D = 1.05$, $F = 1$, $\epsilon = 0.03$, $\beta = 5$, for the second mode $K = 2$.

plane $z = 0$. However, at $t = 4$, the bipolar outflow has clearly been replaced by a unipolar flow with a single jet exiting downward in the picture. Either side of this jet are small recirculating regions resulting from viscous entrainment.

With the choice of density ratio $D = 1.05$ illustrated in this paper, the maximum value of the density perturbation $\bar{\rho}$ is therefore 0.05. Comparisons with the inviscid solutions of Section 2 show that, for early times, the inviscid interface lies roughly along the contour $\bar{\rho} = 0.03$. Figure 4 shows the axi-symmetric surface formed by this contour, for the second-mode solution ($K = 2$), at the later time $t = 5$. The surface clearly still retains some features of its initial bipolar shape, and there are outflows near both poles. But the jet at the bottom of the picture is clearly the larger of the two, and confirms that the mode-one solution has now dominated the outflow shape.

It is evident from Figures 3 and 4 that the mode-one solution ($K = 1$) ultimately dominates as time progresses. This could, perhaps, be inferred from the linearized inviscid result (3.16) which shows that the $K = 1$ mode is the most unstable. Evidently the inclusion of viscosity in the model couples all the modes in a manner that the pure nonlinearity of the inviscid solutions in Figure 2 does not achieve, so allowing a cascade of energy down to this lowest mode. Given its importance in the viscous case, it is therefore worth studying the first-mode solution directly, and this is achieved by setting $K = 1$ in the initial conditions (4.15)–(4.19). In order to improve accuracy in this important case, solutions were obtained with $M = N = 25$ Fourier coefficients and 161 mesh points in the two coordinates r and ϕ.

https://doi.org/10.1017/S1446181112000090 Published online by Cambridge University Press

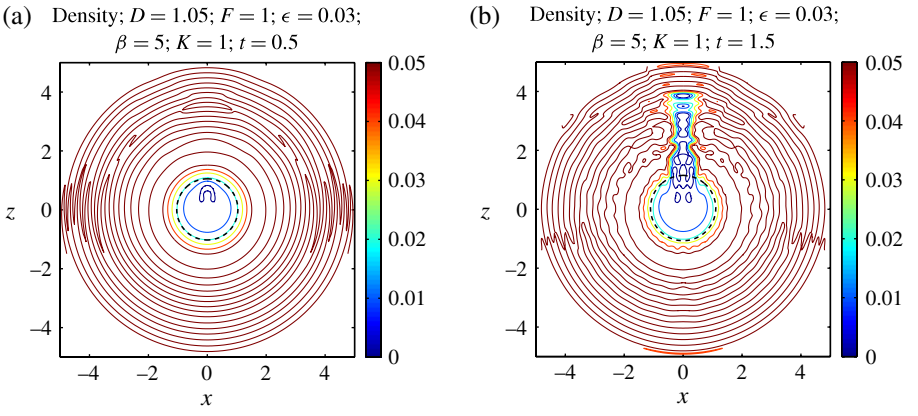

FIGURE 5. A comparison of the viscous and inviscid solutions for the first-mode solution ($K = 1$), at times (a) $t = 0.5$ and (b) $t = 1.5$. Density contours are shown for the viscous solution, and the interface in the inviscid case is shown as a thick dashed line. The scale on both axes is the same.

Two solutions are shown in Figure 5, at the two times $t = 0.5$ and $t = 1.5$ for the case $K = 1$. For the viscous results, contours of the density perturbation function $\bar{\rho}$ are presented, and care has been taken to show the same contour levels $0 < \bar{\rho} < 0.05$ in each diagram, to enable comparison. In addition, the nonlinear interface computed for the inviscid solution at the appropriate time is also overlaid on both diagrams, and is drawn with a thick dashed line.

For the early time $t = 0.5$, there is very close agreement between the inviscid and viscous results, with the inviscid interface lying almost exactly along the contour $\bar{\rho} = 0.02$, as may be seen in Figure 5(a). (There is no significance to the large number of contours shown at the edge of this figure, since they are all representations of $\bar{\rho} = 0.05$. This may be confirmed by reference to the colour bar shown at the right of the figure. Colour available online.) As time increases, the inviscid interface bulges slightly toward the top of the diagram, until at some time a little greater than $t = 1.5$, the curvature at the top pole becomes very large, similar to that shown in Figure 2(b). Beyond that time, the inviscid solution fails, and it appears to be the case that an interfacial curvature singularity is formed there in finite time, analogously to the work of Moore [40]. In the plane Rayleigh–Taylor case, Forbes [21, 22] among many others suggested that the curvature singularity in the inviscid solution was the trigger in the viscous case for the formation of small regions of intense vorticity, and these caused the viscous interface to overturn. In the present three-dimensional geometry, this curvature singularity appears to be associated with jet formation at the lowest mode $K = 1$, and this may be seen in Figure 5(b) at the later time $t = 1.5$. Interestingly, the inviscid interface nevertheless lies almost exactly between the $\bar{\rho} = 0.02$ and $\bar{\rho} = 0.03$ contours almost everywhere, except for the narrow jet region at the top of the figure. Again, it must be remembered that there is no significance to the fact that the jet in this diagram appears at the "top" of the picture instead of at the "bottom" as in Figures 3

https://doi.org/10.1017/S1446181112000090 Published online by Cambridge University Press

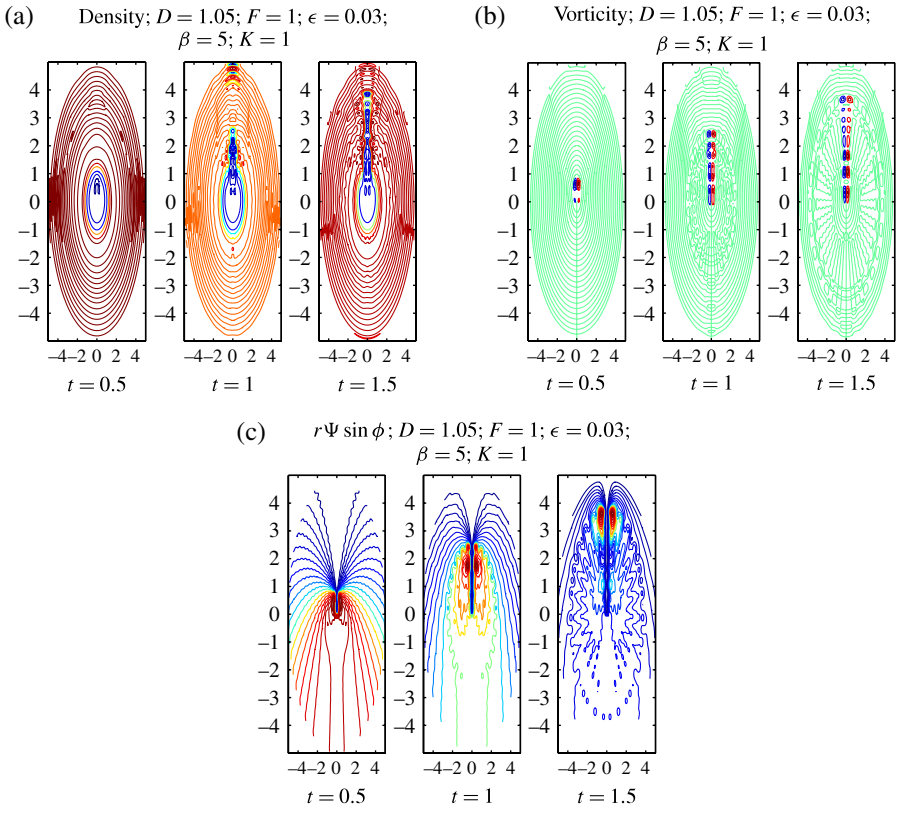

FIGURE 6. The viscous solution at the three times $t = 0.5$, 1, 1.5 for the case $D = 1.05$, $F = 1$, $\epsilon = 0.03$, $\beta = 5$, for the first mode $K = 1$. Solution contours are shown for (a) the density, (b) the vorticity and (c) a variable related to the location of the streamlines.

and 4; since gravity is directed purely radially inward, there is no preferred direction in this sense.

A more detailed view of the evolution of the mode-one jet for these same parameter values is presented in Figure 6, for the three time values $t = 0.5$, 1 and 1.5. In Figure 6(a) density contours are shown, as in Figure 5, and the growth of the jet at the top of these diagrams can be seen. Figure 6(b) presents vorticity contours for these same three times. As with Figure 3(b), the vorticity is zero over almost all of the computational domain, so that this is almost an irrotational flow. However, there is a strong narrow region of vorticity either side of the mode-one jet that forms at the top of these pictures, similar to the behaviour of vorticity in a forced plume (see the paper of Forbes and Hocking [24]). In spherical polar coordinates (2.1), the quantity $r\Psi \sin\phi$ is constant along streamlines in steady flow, and contours of this function are presented in Figure 6(c) for the three times shown. These streamlines start as simple straight lines radially outward from the point source at small times, as expected, but

https://doi.org/10.1017/S1446181112000090 Published online by Cambridge University Press

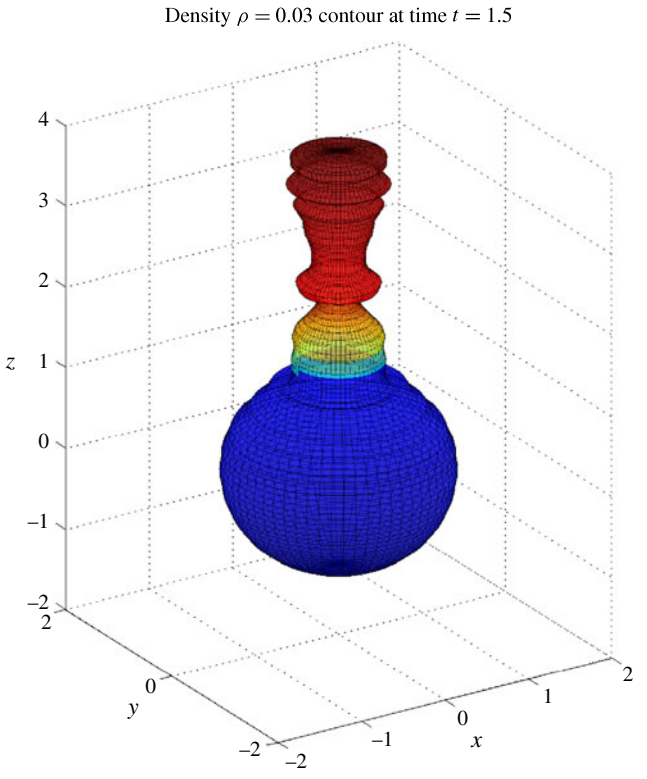

FIGURE 7. The axi-symmetric surface formed by the density contour $\bar{\rho} = 0.03$ in the viscous solution at time $t = 1.5$, for the case $D = 1.05$, $F = 1$, $\epsilon = 0.03$, $\beta = 5$, for the first mode $K = 1$.

quickly develop into an asymmetric jet directed toward the top of the diagram. At the early time $t = 0.5$, there are small wiggles in some of the streamlines far from the point source. These are again a consequence of the sensitivity of the contouring algorithm to very small oscillations in numerical values of Ψ (particularly when multiplied by the radial coordinate r), but they are of no physical significance.

As a further aid to visualization of the mode-one jet, the surface formed by the contour $\bar{\rho} = 0.03$ at time $t = 1.5$ is shown in Figure 7. At the bottom of this diagram, the surface essentially still forms a spherical globe, but there is a strong jet at the top of the region. This axi-symmetric outflow plume possesses a number of small-amplitude wavelets along its length, due to viscous entrainment of the surrounding medium. This is consistent with the patterns of vorticity along the jet, as seen in Figure 6(b).

To conclude this presentation of results, the mode-four solution is considered. This is obtained simply by setting $K = 4$ in the initial conditions (2.37) for the inviscid case and (4.15)–(4.19) for the corresponding viscous solution. The inviscid solution is shown in Figure 8, for the five values of time $t = 1, 2, 3, 4, 5$. Figure 8(a) shows interface profiles at the different times, and the four lobes corresponding to the $K = 4$

https://doi.org/10.1017/S1446181112000090 Published online by Cambridge University Press

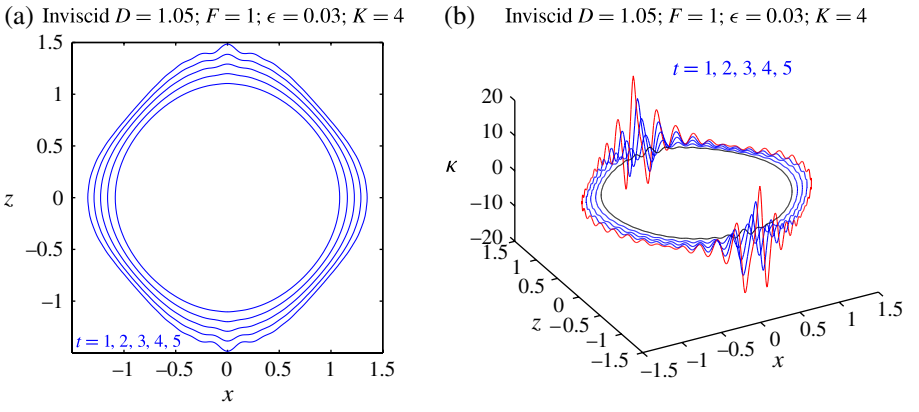

FIGURE 8. The inviscid solution at five different times $t = 1, 2, 3, 4, 5$, computed with parameter values $D = 1.05$, $F = 1$, $\epsilon = 0.03$, for the fourth mode $K = 4$. Results are shown for (a) the interface shape and (b) the curvature. The scale in (a) is the same on both axes.

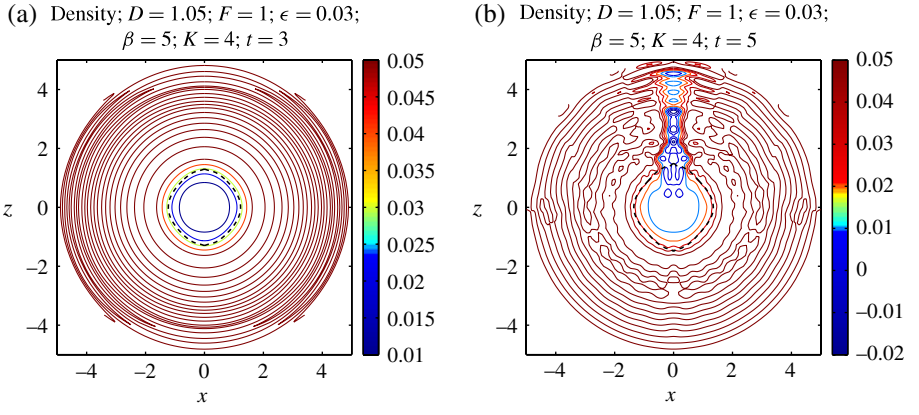

FIGURE 9. A comparison of the viscous and inviscid solutions for the fourth-mode solution ($K = 4$), at times (a) $t = 3$ and (b) $t = 5$. Density contours are shown for the viscous solution, and the interface in the inviscid case is shown as a thick dashed line. The scale on both axes is the same.

solution can be seen clearly. Again, a small region of high curvature develops near the two poles on the z-axis, and eventually these high-curvature regions cause the failure of the numerical method in Section 2, at sufficiently large times. The curvature is shown in Figure 8(b) at the five different times, and the growth of regions of very high curvature near the two poles can be seen in this diagram. The development of Moore curvature singularities [40] within finite time at the interface seems highly likely for these inviscid flows, corresponding to their formation in planar Rayleigh–Taylor flows [21, 22].

In Figure 9, a comparison is made between the predictions of the nonlinear inviscid theory and the Boussinesq viscous result, at the two different times $t = 3$ and $t = 5$. The

https://doi.org/10.1017/S1446181112000090 Published online by Cambridge University Press

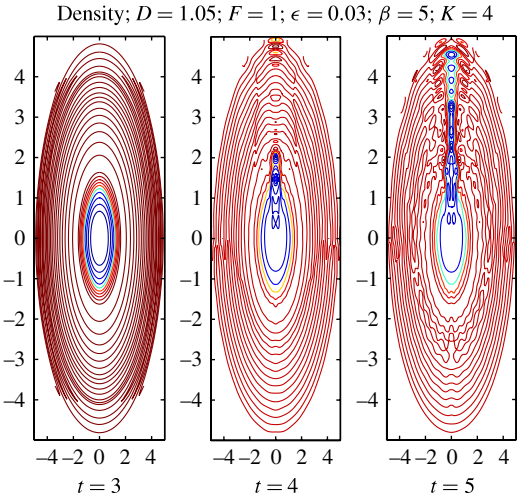

FIGURE 10. Growth of a mode-one type jet in the viscous solution for the mode-four case $K = 4$. Density contours are shown at the three times $t = 3, 4, 5$.

large number of contours at the outer regions of these diagrams is of no significance, and is instead merely an artifice of the contouring routine, since all these contours indicate the same level $\bar{\rho} = 0.05$ of the density perturbation function; this is confirmed by an examination of the colour bar at the right of each diagram (colour available online). At the earlier time $t = 3$ shown in Figure 9(a), there is very close agreement between the viscous and inviscid results, and the interface predicted by the inviscid theory lies almost entirely along the density contour $\bar{\rho} = 0.025$. The density contours for the viscous solution inside that curve also display the four-lobed shape expected for this $K = 4$ fourth-mode solution. At the later time $t = 5$ shown in Figure 9(b), however, a single jet has emerged at the top of the diagram, and has almost reached the edge $r = \beta$ of the computational window (the numerical solution continues to run for later times than this, but is likely to be unreliable for this reason). For this higher-mode solution, it is again evidently the case that the regions of high curvature formed in the inviscid model serve as a trigger in the viscous case for a cascade of energy down to the lowest mode $K = 1$, which is the most unstable; this then results in the formation of a unipolar jet. In spite of this, however, the nonlinear interface at this time $t = 5$ lies very nearly on the density contour $\bar{\rho} = 0.03$ over almost all of the lower section of this figure.

The growth of this single jet out of what was initially a mode-four solution, obtained with $K = 4$, is shown in slightly more detail in Figure 10. Here, density profiles are given at the three times $t = 3$, 4 and 5, and show clearly the evolution of the mode-one jet at the top of the picture. At time $t = 3$, there is close agreement between the viscous and inviscid results, as observed in Figure 9, and at that time both solutions are dominated by the mode-four result, with four outflow lobes arranged

https://doi.org/10.1017/S1446181112000090 Published online by Cambridge University Press

axi-symmetrically around the sphere. However, by time $t = 4$ a single jet begins to emerge, and it grows into a large mode-one jet, similar to that shown in Figure 7, by time $t = 5$.

6. Discussion and conclusion

This paper has examined the outflow of a light fluid from a point source into a surrounding heavier fluid, with an interface separating the two regions. Both fluids are incompressible, and the situation has been modelled for inviscid flows as well as in a Boussinesq viscous sense, in which the two fluids are of comparable density and the interface is approximated by a narrow zone across which the density changes continuously but rapidly. The outflow is unstable due both to Rayleigh–Taylor effects, since a light fluid is pushing a heavier one, and also as a result of Bell–Plesset effects, in which the spherical geometry may serve to destabilize the interface. This is discussed by Epstein [18], and was encountered in Section 3.

The inviscid model has been solved using a spectral technique proposed by Forbes et al. [23], in which the conditions on the interface are used to derive certain identities between the various time-dependent Fourier coefficients in the representations of the solution functions. A strength of this approach is that it allows the interfacial curvature to be obtained accurately, since the required spatial derivatives are evaluated by exact differentiation of the Fourier representations. It has been found that the inviscid outflow is apparently limited by the formation of a curvature singularity on the interface, at the poles, within finite time. This is consistent with the results of Cowley et al. [15] and Moore [40] in planar geometry. A linearized analysis of the inviscid situation, valid for early times when the amplitude of the disturbance is still small, leads to a difficult equation for which no closed-form solution exists. Nevertheless, in the zero-gravity limit $F \to \infty$, the equation has been shown to be equivalent to the evolution equation presented by Mikaelian [39], and in that case it does admit a relatively straightforward solution. This has been compared with the results of the numerical solution of the inviscid problem, and the two are in close agreement for early times, although that comparison has not been presented here in the interest of space.

Viscous effects have also been included in this study, primarily to quantify the effect that viscosity has on the evolving interface. This has been done using a Boussinesq approach adapted from Farrow and Hocking [19]. This has the advantage of simplifying the treatment of the interface between the two fluids, since it approximates the true situation with a single fluid in which the density changes continuously across a narrow interfacial zone. This weakly viscous problem has been solved using a spectral method, and the results are in good agreement with the predictions of the purely inviscid approach for early times. The inviscid theory fails at a critical time due to the formation of curvature singularities on the interface; at about this critical time, the viscous solution undergoes a transition from a state determined by its initial conditions to a state dominated by a mode-one outflow. This consists of a single jet, which may

https://doi.org/10.1017/S1446181112000090 Published online by Cambridge University Press

appear at either pole since gravity is directed purely inward toward the point source, and so neither is preferred in the model equations.

This cascade, in the viscous case, of energy down to the mode-one solution with its single outflow jet, is an unexpected outcome and so has been checked very carefully. To safeguard against numerical instabilities, the solutions have been variously subjected to filtering and to several smoothing algorithms, but these do not change the results. In addition, as an extra check, the nonconstant gravitational body-force term per mass $-(G\mathcal{M}/r^2)\mathbf{e_r}$ used in this paper has been replaced with a simpler constant inwardly directed gravitational term $-g\mathbf{e_r}$ (both given here in dimensional variables), but this has had no significant effect on the outcome.

The qualitative difference between these results for spherical outflow and the planar outflow case discussed by Forbes [22] and Matsuoka and Nishihara [37] is caused precisely by the different geometry in these two cases. This is reflected in the vorticity equation (4.5) by the presence of the additional term $-(\zeta/r)(u + w\cot\phi)$ in the viscous case. A term of this type does not appear in planar geometries. When it is removed (wrongly!) from equation (4.5), results are then obtained that are qualitatively similar to those of Forbes [22] or Matsuoka and Nishihara [37]; there is no preference for mode-one solutions, so that a solution with initial conditions corresponding to mode K remains in that mode throughout its evolution, and viscosity results in large overturning plumes with a mushroom shape. So the convergence of solutions in the viscous case to outflows dominated by mode-one behaviour is a consequence of the inescapably three-dimensional nature of their geometry.

This then raises the question of the relevance of these results in practice. One possible laboratory for outflows of this type might be provided by astrophysical applications. Somewhat in contradiction to the findings of this paper, there are many instances of strongly bipolar flows occurring in astrophysics, as indicated by Stahler and Palla [49, Section 13.2.1] and the review by Zinnecker and Yorke [56]. A particularly intriguing example of these types of outflows is to be found in the remarkable object Eta Carinae, a massive star of probably greater than 100 solar masses, that underwent an enormous eruption in the 1830s. Its bipolar outflow has been imaged using the Hubble Telescope, and is approximately axi-symmetric as assumed in the present paper. A review of work and some ongoing questions about Eta Carinae is presented by Davidson and Humphries [16]. Nevertheless, the role of magnetic fields is perhaps unclear in these situations, and the essentially dipole-like nature of a magnetic source located at the star could certainly promote bipolar outflows of material. The effect of magnetic fields on planar Rayleigh–Taylor flows has recently been investigated by Chambers and Forbes [12], for example, and a similar approach could be adopted in the present application.

Nevertheless, there is a growing body of evidence that one-sided outflows may indeed occur in astrophysics. Some emission jets of this type are discussed in the review by Reipurth and Bally [44], and a recent article by Lovelace et al. [35] presents computational evidence for such behaviour. As observed here, there is no preferred "up" or "down" direction in these flows, so that the one-sided jet could emerge from

https://doi.org/10.1017/S1446181112000090 Published online by Cambridge University Press

either pole. Indeed, Lovelace et al. [35] compute situations, for a rotating star, in which the outflow *switches* from one pole to the other; some possible experimental evidence for this behaviour has recently been reported by Chené and St-Louis [13]. In addition, in the literature on internal confinement fusion, in which spherical implosion occurs, instability can lead to the formation of a long spike jet, as discussed by Ye et al. [53].

The solutions discussed in this paper are all independent of the azimuthal angle θ in the spherical polar coordinate system, with the result that they are rotationally symmetric about the z-axis. Of course, it is also possible to consider outflow types with variations in both angles ϕ and θ. In that case, the axial symmetry would be lost, and extremely complex outflows would be produced, involving fully three-dimensional geometry. In principle, the techniques of the present paper can be adapted to this difficult problem, although the computational requirements would be enormous. Those interesting flows, along with considerations of magnetic field effects, must be left to future investigation.

Acknowledgements

This research has been supported in part by Australian Research Council grant DP1093658. I am grateful to Drs. Andrew Cole and Simon Ellingsen for discussions related to astrophysical outflows. Suggestions from two anonymous referees are also gratefully acknowledged.

Appendix A. ODEs for viscous Fourier coefficients

For completeness, this appendix sets out the systems of ordinary differential equations satisfied by the Fourier coefficients in the Boussinesq viscous model described in Section 4.

The density equation (4.2) is spectrally decomposed, as described in Section 4, and at the zeroth order in angle yields the system

$$\begin{aligned}\frac{dC_{k0}}{dt} = &-\frac{3}{\beta^3}\int_0^\beta\int_0^\pi\left(u\frac{\partial\bar\rho}{\partial r}+\frac{w}{r}\frac{\partial\bar\rho}{\partial\phi}\right)r^2\sin\left(\frac{k\pi r^3}{\beta^3}\right)\sin\phi\,d\phi\,dr\\ &+\frac{72\sigma(D-1)}{\beta^3}\int_0^\beta\left(\frac{r}{\beta}\right)^3\sin\left(\frac{k\pi r^3}{\beta^3}\right)dr\\ &+\frac{6\sigma}{\beta^3}\sum_{m=1}^{M}C_{m0}(t)\Big[12m\pi\int_0^\beta\left(\frac{r}{\beta}\right)^3\cos\left(\frac{m\pi r^3}{\beta^3}\right)\sin\left(\frac{k\pi r^3}{\beta^3}\right)dr\\ &-9m^2\pi^2\int_0^\beta\left(\frac{r}{\beta}\right)^6\sin\left(\frac{m\pi r^3}{\beta^3}\right)\sin\left(\frac{k\pi r^3}{\beta^3}\right)dr\Big],\end{aligned}\tag{A.1}$$

where $k = 1, 2, \ldots, M$. Similarly, the higher-order coefficients $C_{k\ell}$ for the ℓth-mode terms in the angle coordinate are found from the system of differential

https://doi.org/10.1017/S1446181112000090 Published online by Cambridge University Press

equations

$$\frac{dC_{k\ell}}{dt} = -\sigma(\alpha_{\ell,k})^2 C_{k\ell}(t) - \frac{(2\ell+1)}{\beta^2 J^2_{\ell+3/2}(\alpha_{\ell,k}\beta)} \int_0^\beta \int_0^\pi \left(u\frac{\partial\bar{\rho}}{\partial r} + \frac{w}{r}\frac{\partial\bar{\rho}}{\partial\phi}\right)\frac{J_{\ell+1/2}(\alpha_{\ell,k}r)}{r^{3/2}} P_\ell(\cos\phi)\sin\phi\, d\phi\, dr + \frac{2\sigma}{\beta^2 J^2_{\ell+3/2}(\alpha_{\ell,k}\beta)} \sum_{m=1}^{M} C_{m\ell}(t)\Big[6\alpha_{\ell,m}\int_0^\beta J'_{\ell+1/2}(\alpha_{\ell,m}r)J_{\ell+1/2}(\alpha_{\ell,k}r)\, dr + 9\int_0^\beta r^{-1}J_{\ell+1/2}(\alpha_{\ell,m}r)J_{\ell+1/2}(\alpha_{\ell,k}r)\, dr\Big], \tag{A.2}$$

where $k = 1, 2, \ldots, M$ and $\ell = 1, 2, \ldots, N$. The vorticity equation (4.5) is similarly decomposed spectrally, as outlined in Section 4, and leads to the further system of MN ordinary differential equations

$$\frac{dA_{k\ell}}{dt} = -\frac{1}{F^2}C_{k\ell}(t) - \frac{1}{R_e}(\alpha_{\ell,k})^2 A_{k\ell}(t) - \frac{(2\ell+1)}{\ell(\ell+1)\beta^2 J^2_{\ell+3/2}(\alpha_{\ell,k}\beta)} \int_0^\beta \int_0^\pi \Big[\Big(ru\frac{\partial\zeta}{\partial r} + w\frac{\partial\zeta}{\partial\phi}\Big)\sin\phi - \zeta(u\sin\phi + w\cos\phi)\Big] r^{1/2} J_{\ell+1/2}(\alpha_{\ell,k}r) P'_\ell(\cos\phi)\sin\phi\, d\phi\, dr, \tag{A.3}$$

where $k = 1, 2, \ldots, M$ and $\ell = 1, 2, \ldots, N$.

This large system of $M(2N + 1)$ equations is now integrated forward in time to give the solution for the Boussinesq viscous model.

References

[1] M. Abramowitz and I. A. Stegun (eds.), *Handbook of mathematical functions: with formulas, graphs and mathematical tables* (Dover Publications, New York, 1972).

[2] P. Amendt, "Bell–Plesset effects for an accelerating interface with contiguous density gradients", *Phys. Plasmas* **13** (2006) 042702; doi:10.1063/1.2174718.

[3] M. J. Andrews and S. B. Dalziel, "Small Atwood number Rayleigh–Taylor experiments", *Phil. Trans. R. Soc. A* **368** (2010) 1663–1679; doi:10.1098/rsta.2010.0007.

[4] K. A. Atkinson, *An introduction to numerical analysis* (John Wiley & Sons, New York, 1978).

[5] G. R. Baker and J. T. Beale, "Vortex blob methods applied to interfacial motion", *J. Comput. Phys.* **196** (2004) 233–258; doi:10.1016/j.jcp.2003.10.023.

[6] G. Baker, R. E. Caflisch and M. Siegel, "Singularity formation during Rayleigh–Taylor instability", *J. Fluid Mech.* **252** (1993) 51–78; doi:10.1017/S0022112093003660.

[7] G. R. Baker and L. D. Pham, "A comparison of blob methods for vortex sheet roll-up", *J. Fluid Mech.* **547** (2006) 297–316; doi:10.1017/S0022112005007305.

[8] G. R. Baker and C. Xie, "Singularities in the complex physical plane for deep water waves", *J. Fluid Mech.* **685** (2011) 83–116; doi:10.1017/jfm.2011.283.

[9] G. K. Batchelor, *An introduction to fluid dynamics* (Cambridge University Press, Cambridge, 1967).

https://doi.org/10.1017/S1446181112000090 Published online by Cambridge University Press

[10] G. Berthoud, "Vapor explosions", *Ann. Rev. Fluid Mech.* **32** (2000) 573–611; doi:10.1146/annurev.fluid.32.1.573.
[11] A. C. Calder *et al*., "On validating an astrophysical simulation code", *Astrophys. J. Suppl. Ser.* **143** (2002) 201–229; doi:10.1086/342267.
[12] K. Chambers and L. K. Forbes, "The magnetic Rayleigh–Taylor instability for inviscid and viscous fluids", *Phys. Plasmas* **18** (2011) 052101; doi:10.1063/1.3574370.
[13] A.-N. Chené and N. St-Louis, "Large-scale periodic variability of the wind of the Wolf–Rayet star WR 1 (HD 4004)", *Astrophys. J.* **716** (2010) 929–941; doi:10.1088/0004-637X/716/2/929.
[14] A. W. Cook and P. E. Dimotakis, "Transition stages of Rayleigh–Taylor instability between miscible fluids", *J. Fluid Mech.* **443** (2001) 69–99; doi:10.1017/S0022112001005377.
[15] S. J. Cowley, G. R. Baker and S. Tanveer, "On the formation of Moore curvature singularities in vortex sheets", *J. Fluid Mech.* **378** (1999) 233–267; doi:10.1017/S0022112098003334.
[16] K. Davidson and R. M. Humphries, "Eta Carinae and its environment", *Ann. Rev. Astron. Astrophys.* **35** (1997) 1–32; doi:10.1146/annurev.astro.35.1.1.
[17] R. Dgani and N. Soker, "Instabilities in moving planetary nebulae", *Astrophys. J.* **495** (1998) 337–345; doi:10.1086/305257.
[18] R. Epstein, "On the Bell–Plesset effects: the effects of uniform compression and geometrical convergence on the classical Rayleigh–Taylor instability", *Phys. Plasmas* **11** (2004) 5114–5124; doi:10.1063/1.1790496.
[19] D. E. Farrow and G. C. Hocking, "A numerical model for withdrawal from a two-layer fluid", *J. Fluid Mech.* **549** (2006) 141–157; doi:10.1017/S0022112005007561.
[20] M. A. Fontelos and F. de la Hoz, "Singularities in water waves and the Rayleigh–Taylor problem", *J. Fluid Mech.* **651** (2010) 211–239; doi:10.1017/S0022112009992710.
[21] L. K. Forbes, "The Rayleigh–Taylor instability for inviscid and viscous fluids", *J. Eng. Math.* **65** (2009) 273–290; doi:10.1007/s10665-009-9288-9.
[22] L. K. Forbes, "A cylindrical Rayleigh–Taylor instability: radial outflow from pipes or stars", *J. Eng. Math.* **70** (2011) 205–224; doi:10.1007/s10665-010-9374-z.
[23] L. K. Forbes, M. J. Chen and C. E. Trenham, "Computing unstable periodic waves at the interface of two inviscid fluids in uniform vertical flow", *J. Comput. Phys.* **221** (2007) 269–287; doi:10.1016/j.jcp.2006.06.010.
[24] L. K. Forbes and G. C. Hocking, 'Unsteady plumes in planar flow of viscous and inviscid fluids', *IMA J. Appl. Math.*, to appear; doi:10.1093/imamat/hxr045.
[25] L. K. Forbes and G. C. Hocking, "Unsteady draining flows from a rectangular tank", *Phys. Fluids* **19** (2007) 082104; doi:10.1063/1.2759891.
[26] I. S. Gradshteyn and I. M. Ryzhik, *Tables of integrals, series and products*, 6th edn (Academic Press, San Diego, CA, 2000).
[27] T. Y. Hou, J. S. Lowengrub and M. J. Shelley, "Boundary integral methods for multicomponent fluids and multiphase materials", *J. Comput. Phys.* **169** (2001) 302–362; doi:10.1006/jcph.2000.6626.
[28] N. A. Inogamov, *The role of Rayleigh–Taylor and Richtmyer–Meshkov instabilities in astrophysics: an introduction*, Volume 10 of *Astrophysics and Space Physics Reviews* (Harwood Academic, Amsterdam, 1999).
[29] R. Krasny, "Desingularization of periodic vortex sheet roll-up", *J. Comput. Phys.* **65** (1986) 292–313; doi:10.1016/0021-9991(86)90210-X.
[30] E. Kreyszig, *Advanced engineering mathematics*, 9th edn (John Wiley & Sons, Hoboken, NJ, 2006).
[31] H. J. Kull, "Theory of the Rayleigh–Taylor instability", *Phys. Rep.* **206** (1991) 197–325; doi:10.1016/0370-1573(91)90153-D.
[32] C. C. Kuranz, R. P. Drake, M. J. Grosskopf, B. Fryxell, A. Budde, J. F. Hansen, A. R. Miles, T. Plewa, N. Hearn and J. Knauer, "Spike morphology in blast-wave driven instability experiments", *Phys. Plasmas* **17** (2010) 052709; doi:10.1063/1.3389135.
[33] J. Lazier, R. Pickart and P. Rhines, "Deep convection", in: *Ocean circulation and climate: observing and modelling the global ocean*, Volume 77 of *International Geophysics Series* (eds G. Siedler, J. Church and J. Gould), (Academic Press, San Diego, CA, 2001) 387–400.

[34] H. Lin, B. D. Storey and A. J. Szeri, "Rayleigh–Taylor instability of violently collapsing bubbles", *Phys. Fluids* **14** (2002) 2925–2928; doi:10.1063/1.1490138.
[35] R. V. E. Lovelace, M. M. Romanova, G. V. Ustyugova and A. V. Koldoba, "One-sided outflows/jets from rotating stars with complex magnetic fields", *Mon. Not. R. Astron. Soc.* **408** (2010) 2083–2091; doi:10.1111/j.1365-2966.2010.17284.x.
[36] M.-M. Mac Low and R. McCray, "Superbubbles in disk galaxies", *Astrophys. J.* **324** (1988) 776–785; doi:10.1086/165936.
[37] C. Matsuoka and K. Nishihara, "Analytical and numerical study on a vortex sheet in incompressible Richtmyer–Meshkov instability in cylindrical geometry", *Phys. Rev. E* **74** (2006) 066303; doi:10.1103/PhysRevE.74.066303.
[38] N. M. McClure-Griffiths, J. M. Dickey, B. M. Gaensler and A. J. Green, "Loops, drips, and walls in the galactic chimney GSH 277+00+36", *Astrophys. J.* **594** (2003) 833–843; doi:10.1086/377152.
[39] K. O. Mikaelian, "Rayleigh–Taylor and Richtmyer–Meshkov instabilities and mixing in stratified cylindrical shells", *Phys. Fluids* **17** (2005) 094105; doi:10.1063/1.2046712.
[40] D. W. Moore, "The spontaneous appearance of a singularity in the shape of an evolving vortex sheet", *Proc. R. Soc. A* **365** (1979) 105–119; doi:10.1098/rspa.1979.0009.
[41] E. A. Neil and G. A. Houseman, "Rayleigh–Taylor instability of the upper mantle and its role in intraplate orogeny", *Geophys. J. Int.* **138** (1999) 89–107; doi:10.1046/j.1365-246x.1999.00841.x.
[42] P. Ramaprabhu, G. Dimonte, Y.-N. Young, A. C. Calder and B. Fryxell, "Limits of the potential flow approach to the single-mode Rayleigh–Taylor problem", *Phys. Rev. E* **74** (2006) 066308; doi:10.1103/PhysRevE.74.066308.
[43] L. Rayleigh, "Investigation of the character of the equilibrium of an incompressible heavy fluid of variable density", *Proc. Lond. Math. Soc.* **14** (1882) 170–177; doi:10.1112/plms/s1-14.1.170.
[44] B. Reipurth and J. Bally, "Herbig–Haro flows: probes of early stellar evolution", *Ann. Rev. Astron. Astrophys.* **39** (2001) 403–455; doi:10.1146/annurev.astro.39.1.403.
[45] R. Scardovelli and S. Zaleski, "Direct numerical simulation of free-surface and interfacial flow", *Ann. Rev. Fluid Mech.* **31** (1999) 567–603; doi:10.1146/annurev.fluid.31.1.567.
[46] K. Shariff, "Fluid mechanics in disks around young stars", *Ann. Rev. Fluid Mech.* **41** (2009) 283–315; doi:10.1146/annurev.fluid.010908.165144.
[47] D. H. Sharp, "An overview of Rayleigh–Taylor instability", *Physica D* **12** (1984) 3–18; doi:10.1016/0167-2789(84)90510-4.
[48] J. Shi, Y.-T. Zhang and C.-W. Shu, "Resolution of high order WENO schemes for complicated flow structures", *J. Comput. Phys.* **186** (2003) 690–696; doi:10.1016/S0021-9991(03)00094-9.
[49] S. W. Stahler and F. Palla, *The formation of stars* (Wiley-VCH, Weinheim, 2004).
[50] G. Taylor, "The instability of liquid surfaces when accelerated in a direction perpendicular to their planes. I", *Proc. R. Soc. A* **201** (1950) 192–196; doi:10.1098/rspa.1950.0052.
[51] G. Tryggvason, W. J. A. Dahm and K. Sbeih, "Fine structure of vortex sheet rollup by viscous and inviscid simulation", *J. Fluids Eng.* **113** (1991) 31–36; doi:10.1115/1.2926492.
[52] G. von Winckel, "Legendre–Gauss quadrature weights and nodes", 2004, http://www.mathworks.com/matlabcentral/fileexchange/4540.
[53] W.-H. Ye, L.-F. Wang and X.-T. He, "Jet-like long spike in nonlinear evolution of ablative Rayleigh–Taylor instability", *Chin. Phys. Lett.* **27** (2010) 125203; doi:10.1088/0256-307X/27/12/125203.
[54] Y.-N. Young and F. E. Ham, "Surface tension in incompressible Rayleigh–Taylor mixing flow", *J. Turbulence* **7** (2006) 1–23; doi:10.1080/14685240600809979.
[55] H. Yu and D. Livescu, "Rayleigh–Taylor instability in cylindrical geometry with compressible fluids", *Phys. Fluids* **20** (2008) 104103; doi:10.1063/1.2991431.
[56] H. Zinnecker and H. W. Yorke, "Toward understanding massive star formation", *Ann. Rev. Astron. Astrophys.* **45** (2007) 481–563; doi:10.1146/annurev.astro.44.051905.092549.